IEEE Access
Multidisciplinary | Rapid Review | Open Access Journal

Received 17 July 2023, accepted 3 August 2023, date of publication 7 August 2023, date of current version 16 August 2023.

Digital Object Identifier 10.1109/ACCESS.2023.3303335

APPLIED RESEARCH

A Novel Scheme of High-Precision Heart Rate Detection With a mm-Wave FMCW Radar

MIN ZHOU[1], YUNXUE LIU[1], SHIE WU[1], CHENGYOU WANG[2], (Member, IEEE), ZEKUN CHEN[1], (Member, IEEE), AND HONGFEI LI[1]

[1]School of Physics and Electronic Information, Yantai University, Yantai 264005, China
[2]School of Mechanical, Electrical and Information Engineering, Shandong University, Weihai 264209, China

Corresponding author: Yunxue Liu (sdytrslyx@vip.163.com)

This work was supported in part by the National Natural Science Foundation of China under Grant 62201491, and in part by the Shandong Provincial Natural Science Foundation under Grant ZR2021QF097.

ABSTRACT Millimeter wave (mm-Wave) radar has been widely employed for non-contact vital sign detection. This research proposes a novel processing scheme to improve the accuracy and stability of non-contact heart rate detection. Firstly, we propose an adaptive range bin selection method based on variance which can select accurate range bins containing phase information of vital signs. Secondly, the smooth spline is utilized to fit the original phase signal to obtain a relatively pure template signal. Subsequently, the pure template signal is used as the input signal for the matched filter to convolve with the phase signal. The matched filtering can eliminate interference and noise such as breathing and random body movements (RBM). Next, the heartbeat signal is extracted by the Variable Mode Extraction (VME) algorithm. Finally, a novel frequency measurement technique named as Double-Chirp Z-Transform (Double-CZT) is proposed. The frequency of the heartbeat signal is measured by the Double-CZT. Compared with the traditional frequency measurement techniques, the Double-CZT improves the accuracy of frequency measurement and allows for more accurate heart rate measurements. Many subjects were invited to participate in the experiment, and the mean absolute error (MAE) of heart rate was less than 1 beat per minute (bpm) on average. The experimental results demonstrate that the proposed scheme can improve the signal-to-noise ratio (SNR) of heartbeat signal and provide accurate heart rate estimation.

INDEX TERMS CZT, frequency measurement technique, matched filtering, non-contact heart rate detection, range bin selection, smooth spline fitting, VME.

I. INTRODUCTION

Heart rate, being an indicator of heart activity, has been recognized as a reliable measure of mental stress [1], arrhythmia, alcohol consumption [2], and drowsiness [3]. With the increasing prevalence of chronic health conditions among young individuals and the elderly population, there is a growing demand for long-term health monitoring [4], [5], [6]. Continuous monitoring of vital signs in drivers has also become crucial for reducing the occurrence of traffic accidents. Furthermore, during natural disasters, the ability to detect heartbeat information through obstacles such as stones and walls plays a vital role in locating and rescuing victims [7].

Traditional methods for heart rate detection primarily fall into two categories: sensor-based methods [8] and vision-based methods [9]. The former belongs to the contact heart rate detection method, which involves direct contact with the subject using electrodes, sensors, etc. However, wearing contact sensors for extended periods can cause discomfort to the subject. Moreover, contact-based detection methods are limited in their applicability to certain individuals with conditions such as skin diseases and burns. The latter enables non-contact heart rate detection, allowing for remote monitoring of vital signs without physical contact with the subject. However, these methods have limitations in

The associate editor coordinating the review of this manuscript and approving it for publication was Hasan S. Mir.

environments with smoke or poor lighting, as they may result in poor performance. Additionally, concerns related to user privacy may arise with the use of vision-based methods.

With the development of integrated circuit and radar technology [10], radar has been applied to the field of vital signs detection, which is an important innovation of radar technology in the medical field. Compared with the traditional non-contact detection technology, the radar-based non-contact vital signs detection technology has stronger penetration ability and anti-interference ability. Furthermore, radar-based detection eliminates concerns regarding user privacy. At present, research on non-contact vital signs detection based on radar mainly includes two categories: 1) Optimize hardware devices such as antennas to suppress noise and improve signal quality. 2) Design and optimize software-level algorithms in vital signs signal processing to enhance the accuracy and reliability of vital signs detection [11].

In general, the radars used for non-contact vital signs detection mainly include continuous wave (CW) radar, impulse ultrawideband (UWB) radar, and frequency-modulated continuous-wave (FMCW) radar. CW radar offers high precision in displacement measurement but lacks ranging capability and is susceptible to noise [12]. UWB radar provides high-range resolution and exhibits strong anti-interference ability. However, it has limitations in frequency utilization and requires a high sampling rate [13]. In comparison, FMCW radar combines the benefits of CW radar and UWB radar. It offers the sensitivity of CW radar and the ranging ability of UWB radar while also being compact and lightweight [14]. Many existing works have verified the feasibility of heartbeat rate detection using FMCW radar [15], [16], [17]. During the existing non-contact heartbeat rate detection process based on FMCW radar, there are three primary factors that influence the accuracy of heart rate estimation: 1) The selection of range bins where the human target is located. 2) The removal of interference and noise such as respiratory harmonics, cross-tuned signals, and random body movements (RBM). 3) The accuracy of frequency measurement method used for the extracted heartbeat signal. These factors must be carefully considered during the heart rate detection process.

To tackle these challenges, this paper proposes a novel scheme that includes three new methods for heart rate detection based on 77 GHz FMCW radar. Firstly, the transmit signal and the echo signal are mixed to generate the intermediate frequency (IF) signal. Subsequently, after Range fast Fourier transform (Range-FFT) for the IF signal, a static signal-clutter removal technique is employed to eliminate the interference of static clutter. Secondly, an adaptive range bin selection method is proposed, which can adaptively select the range bin that contains the vital sign information. Then, the method of matched filtering based on smooth spline fitting is employed to remove the interference and noise. Based on the fitting method, combined with matched filtering technology, the signal-to-noise ratio (SNR) of the heartbeat signal can be further improved. Next, the Variable Mode Extraction (VME) algorithm is used to extract the heartbeat signal. Finally, a novel frequency measurement method, Double-Chirp Z-Transform (Double-CZT), is proposed to achieve high accuracy frequency measurement in a short time window, enabling real-time heart rate detection.

The remaining sections are organized as follows. We review the related works in Section II. Section III presents the basic principles of vital sign measurement based on FMCW. The proposed method is described in Section IV. Experiments, results, and conclusion are provided in Section V, VI, and VII, respectively.

II. RELATED WORK

One of the advantages of millimeter wave (mm-Wave) FMCW radar is its high precision and ability to detect millimeter-scale motion, making it suitable for vital signs detection in various scenarios. This part will introduce the related work of vital signs detection using mm-Wave FMCW radar from three aspects.

A. mm-WAVE RADAR IMAGING

Traditional optical imaging systems are known for their complexity, high cost, vulnerability to environmental conditions and lighting, and potential infringement on personal privacy. In contrast, mm-Wave radar imaging systems compensate for the shortcomings and limitations of optical imaging systems, making them emerged as the preferred choice for imaging systems. Additionally, the mm-Wave radar can offer high-resolution 3D point cloud representations that can be locally processed using edge artificial intelligence (AI) algorithms to reconstruct human motion. However, challenges exist due to factors such as a smaller number of radar antennas and wide beam width, which can lead to low angular resolution and difficulty in distinguishing targets. In 2020, Texas Instruments (TI) launched cascaded imaging radar, which employs hundreds of virtual channels with an azimuth resolution as low as 1.4 degrees. To improve the accurate perception, Danzer et al. utilized PointNets for 2D object detection based on point cloud from mm-Wave radar [18]. Singh et al. [19] present a human activity recognition approach using 77 GHz TI IWR1443 mm-Wave radar, achieving over 90% accuracy in distinguishing five different activities.

B. mm-WAVE RADAR FOR HEALTH-RELATED APPLICATIONS

The experience of the COVID-19 pandemic has highlighted the significance of home rehabilitation and health monitoring systems. An and Ogras proposed the mm-Wave-based Assistive Rehabilitation System (MARS), which employs convolution neural network (CNN) to estimate the location of the human dimension. MARS can reconstruct 19 human joints and their skeleton from the point cloud generated by mm-Wave radar with an average mean absolute error of 5.87 cm [20]. mm-Wave point cloud technology can provide valuable information, including distance, speed, and angle of the target, enabling accurate determination of the location and

status of the human body. Remote fall detection for the elderly has emerged as a significant research direction. Ding et al. developed a fall detection system that accurately detects fall incidents and distinguishes the direction of the fall with an accuracy rate exceeding 90% [21]. Additionally, mm-Wave radar can be utilized for non-contact heart rate detection. A robot-mounted mm-Wave radar system was proposed to periodically measure heart rate under various user poses in [17], The system can also estimate heart rate from the lower leg while providing an estimation uncertainty.

C. HEART MONITORING ALGORITHMS

The solution for non-contact detection of vital signs based on mm-Wave radar primarily consists of four modules: signal preprocessing, interference and noise removal, signal decomposition, and heart rate measurement [16].

The main objective of the signal preprocessing process is to extract phase signals that contain vital sign information from the range bin where the target is located. There are two primary classic range bin selection approaches based on energy and variance [22]. The first approach is based on the fact that periodic movement of the human thorax generated by heartbeat, respiration, etc., constitutes the majority of the space's dynamic component. As a result, the range bin with the maximum energy inside the radar echo signal matrix can be chosen as the target bin [16], [23]. The second approach is based on the echo signal reflected from non-target objects, which has time-invariant properties and has been significantly attenuated by static clutter filtering. On the other hand, the echo signal emitted from the human body fluctuates significantly, with the variance increasing as the fluctuation increases. Therefore, the target bin can be calculated by variance. Most previous radar-based heart rate measurement methods have assumed that the human target is located at a fixed range bin [24]. However, the accuracy of the above methods may be significantly affected by RBM and the target's considerable respiration. These factors can cause the range bin where the target is located to change, leading to potential inaccuracies in the estimation [25].

The chest displacement caused by vital signs is a small movement of a few centimeters or even a few millimeters. Therefore, interference and noise such as large-scale RBM will destroy vital signs and greatly reduce the accuracy of heart rate detection [23], [26]. In 2016, Ferrears tackled the interference problem caused by RBM in the vital sign detection based on FMCW radar by the processing which installs one radar in front and one radar behind the human body. This processing reduces the interference of RBM by adding two radars IF signals [27]. However, the two radars system need to be measured synchronously, which is difficult to configure parameters and realize in actual measurement. TI segmented the phase data by applying a threshold to determine whether the data falls within the range of heart rate variation. Data that does not fit within this range, indicating potential damage caused by exercise, is discarded [16]. However, the discarded data may potentially contain valuable information about an individual's health status, including indicators of heart disease. Additionally, discarding this data can lead to a loss of data continuity, making it challenging to perform dynamic analysis of heartbeat changes. Lv.et al devised the matched filtering technology to restore the damaged vital sign signal by eliminating noise efficiently [26]. However, the effectiveness of this method is contingent on the purity of the selected template signal. F. Wang and colleagues employed B-spline fitting to suppress motion artifacts and obtain a clean phase signal that reveals vital sign information [28], [29]. However, only using the fitting method can easily lead to excessive loss of valuable components in the original phase signal or incomplete removal of human motion components.

The frequencies of respiratory and heartbeat signals of healthy adults in the calm state often lie in [0.12, 0.5] Hz and [0.8, 2] Hz [30], respectively. At present, many time domain and frequency domain methods have been proposed to extract heartbeat signals. Reference [31] and TI [16] extract heartbeat signals through a filter with a cutoff frequency range of [0.8, 2] Hz. However, the heartbeat signal obtained by this method will be affected by respiratory harmonics, which will affect the accuracy of heart rate estimation. In the current study, the mode decomposition methodology is another method to extract the heartbeat signal from the composite cardiopulmonary signal. At present, the common mode decomposition methods are Empirical Mode Decomposition (EMD), Ensemble Empirical Mode Decomposition (EEMD), and Complete Ensemble Empirical Mode Decomposition with Adaptive Noise (CEEMDAN), etc., which decompose the cardiopulmonary signal into multiple Intrinsic Mode Functions (IMFs) [32], [33], [34]. However, they all have different degrees of modal aliasing and noise residual problems. In addition, Variational Mode Decomposition (VMD) is also used to monitor the heart rate of people in a static state [35], [36]. However, due to the strong interference of respiratory signal, the obtained IMF of heartbeat signal still contains residuals related to respiration and its harmonics, which affects the detection of heart rate. Mingxu Xiang presented a fast Fourier transform-Chirp Z-Transform (FFT-CZT) method for high-precision frequency measurement and used a notch filter to remove the respiration interference by filtering the respiration harmonics [37]. However, the heartbeat signal may be eliminated simultaneously with the respiratory harmonics.

Selecting a high-precision spectrum estimation method is crucial for accurately estimating the frequency of heartbeat signals. The fast Fourier transform (FFT) algorithm is widely used in large datasets and real-time applications due to its efficiency in calculating signal spectrum. However, its estimation accuracy is limited. Reference [38] utilized the Multiple Signal Classification (MUSIC) algorithm to measure the frequency of heartbeat signal. The MUSIC algorithm is a super-resolution method that can effectively distinguish multiple signals with close frequencies and accurately estimate signal frequencies. Nonetheless, the MUSIC algorithm's spectrum search relies on grid search [39], which poses significant computational challenges and is difficult to

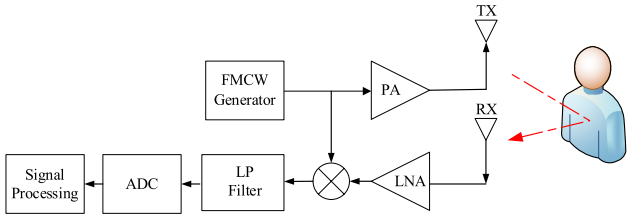

FIGURE 1. FMCW radar system block diagram.

implement in real-time scenarios. Another common alternative is the Chirp Z-Transform (CZT) algorithm [37], which can analyze a specific frequency band of the signal with high resolution. It is relatively simpler to implement and has lower computational complexity. However, the CZT algorithm is more susceptible to the influence of noise.

On the basis of the TI vital sign detection scheme, the aforementioned schemes contribute differently to signal preprocessing, interference and noise removal, signal decomposition, and heart rate frequency estimation. In comparison, the scheme proposed in this paper can achieve high-precision heart rate detection even in the presence of RBM. Firstly, our novel range bin selection method in signal preprocessing accurately selects range bins containing human vital sign information with less calculation. Secondly, based on the smooth spline fitting method, combined with matched filtering technology, we address the potential issues of underfitting and overfitting in the fitting process. Thirdly, the VME algorithm effectively separates heartbeat signal from the background noise and interference under low computational complexity. Finally, utilizing Double-CZT for measuring heartbeat signal can further improve the accuracy of heart rate detection.

III. SYSTEM OVERVIEW AND THEORETICAL MODEL

A. SYSTEM OVERVIEW

The FMCW radar system consists of several components, including a signal generator, power amplifier (PA), low-noise amplifier (LNA), low-pass (LP) filter, and analog-to-digital converter (ADC) module [40]. The simplified block diagram of this system is shown in Fig. 1. In the radar front-end, the signal generator produces the FMCW signal, which is then amplified by the PA and transmitted through the transmitting antenna. The receiving antenna receives the echo signal from the target, which is subsequently mixed with the local array signal after amplification by the LNA, resulting in the IF signal [7].

B. THEORETICAL MODEL

The chirp signal emitted by the FMCW radar is:

$$s(t) = A_t \exp\left[j\left(2\pi f_{\min} t + \pi K t^2\right)\right], 0 < t < T_r \quad (1)$$

where $f_{\min}$ is the starting frequency of the chirp signal, A_t is the amplitude related to the transmitting power, and K is a positive linear scanning frequency. Assuming that the initial distance between the human target and the radar is R_0, when the human target remains relatively stationary and the micro-movement of the body surface caused by breathing and heartbeat is $x(t)$, then the real-time distance between the human target and the radar is $R(t) = R_0 + x(t)$. The echo signal reflected from the human target and modulated by the thoracic motion will have a delay of $\tau = 2R(t)/c$ concerning $s(t)$ and c is the speed of light. Neglecting the effects of thermal noise and other channel factors, mixing the transmit signal with the echo signal to obtain the IF signal can be simplified as [41]:

$$y(t) \approx A_t A_r \exp\left(j\left(\phi(t) + w_b t\right)\right), \tau < t < T_r \quad (2)$$

$$w_b = 4\pi \frac{KR_0}{c} \quad (3)$$

$$\phi(t) = 4\pi \frac{R_0 + x(t)}{\lambda_{\max}} \quad (4)$$

where w_b is the frequency of the IF signal, and $\phi(t)$ is the phase of the IF signal. It can be seen that $\phi(t)$ varies with $x(t)$ relative to $\lambda_{\max}$ and the higher the operating frequency of radar, the higher the sensitivity.

To obtain $x(t)$, we apply the FFT to the IF signal. Each Range-FFT bin corresponds to a specific distance with an associated phase similar to $\phi(t)$. Several chirps are transmitted consecutively to capture time-varying signals, which is equivalent to the sampling of $x(t)$. As a result, by extracting the phase from the Range-FFT bins that correspond to the subject, we can retrieve information about physiological vibrations.

IV. METHODOLOGY

In this paper, we propose a novel scheme for non-contact heart rate measurement based on FMCW radar. The main processing flow, as illustrated in Fig. 2, consists of the following steps: radar signal acquisition, signal preprocessing, noise removal, signal decomposition, and heart rate measurement. Signal preprocessing mainly comprises Range-FFT, static signal-clutter removal, range bin selection, phase extraction, phase unwrapping, phase difference, and impulse noise removal. At first, the transmitted radar signal is mixed with the echo signal, producing the IF signal, which is then sampled by ADC to generate a two-dimensional matrix. The matrix rows correspond to sampled data for each chirp, and the columns are composed of different frames. These sampled data undergo preprocessing to obtain the preprocessing signal. Subsequently, interference and noise such as breathing and RBM are removed by the method of matched filtering based on smooth spline fitting. The VME algorithm is then employed to obtain the heartbeat signal from the output signal of matched filter. Finally, the heart rate is determined by measuring the frequency of the extracted heartbeat signal using the newly proposed Double-CZT method. Each step of the process is detailed below in further depth.

A. METHODS USED IN SIGNAL PREPROCESSING

1) STATIC SIGNAL-CLUTTER REMOVAL

Assuming that the number of sampled chirps is N and the number of samples per chirp is M, this results in a raw

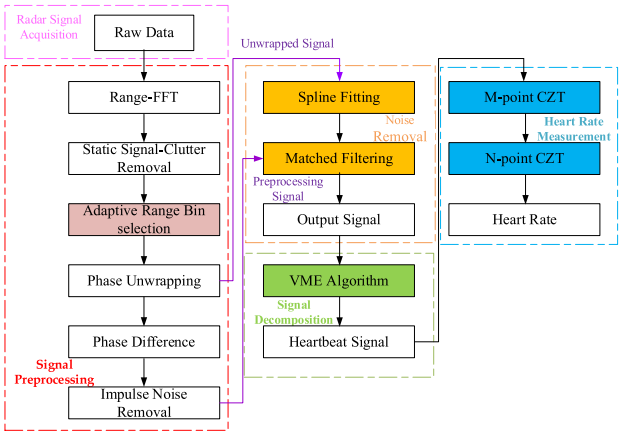

FIGURE 2. Block diagram for heart rate monitoring based on FMCW radar.

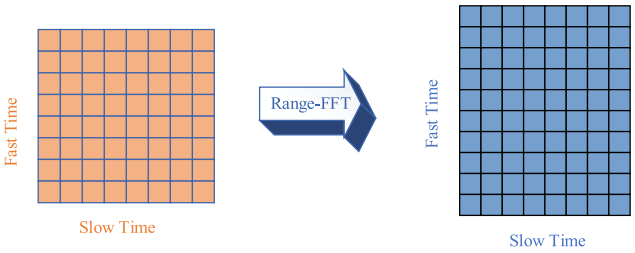

FIGURE 3. The data matrix after Range-FFT.

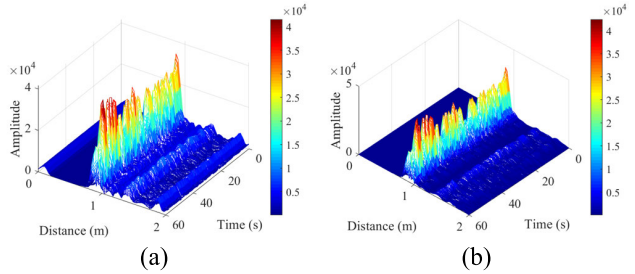

FIGURE 4. Echo pulse 3D distance image: (a) Before static signal-clutter removal; (b) After static signal-clutter removal.

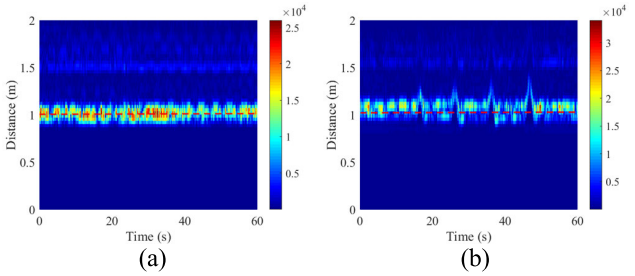

FIGURE 5. Samples of date matrix (stable vs. unstable): (a) Stable state; (b) Unstable state caused by RBM.

AD data matrix of size $M \times N$. Range-FFT is employed for each chirp to obtain the range bins corresponding to the human target chest cavity. Following the Range-FFT, the $M' \times N$ dimensional spectrum data matrix $\mathbf{R}$ is generated [42]. In this matrix, the horizontal coordinate represents the time dimension, i.e., the slow time dimension; the vertical coordinate represents the distance dimension, i.e., the fast time dimension. The data matrix after Range-FFT is shown in Fig. 3.

The data matrix contains multiple reflections from stationary objects, generating a strong fixed DC component in the returned signal. To extract reliable vital sign data from the data matrix, it is necessary to remove the background noise. Assuming a static signal propagation environment where the human target is the only source of motion, the average value of each row in the matrix is calculated to represent the static clutter. Subsequently, this average value is subtracted from each row of the matrix that contains information about chest motion. After eliminating the static noise, the signal matrix is represented as follows:

$$\mathbf{R}'[m,n] = \mathbf{R}[m,n] - \frac{1}{N}\sum_{n=1}^{N}\mathbf{R}[m,n] \tag{5}$$

where $m = 1, 2 \cdots, M'$ and $n = 1, 2, \cdots, N$. A schematic representation of the distance-time matrix before and after the removal of static clutter is depicted in Fig. 4. It can be noticed that there are many false peaks in Fig. 4(a). However, in Fig. 4(b), after static signal-clutter removal, the range bins where the human target is located are more clearly displayed.

2) PROPOSED ADAPTIVE RANGE BIN SELECTION

The vertical coordinates of the data matrix $\mathbf{R}$ represent the distance information of a target. Once the radar module and its configuration file are determined, the distance represented by each range bin remains fixed. The targets sat approximately 1 m in front of the radar in the experiment. One target remained stationary while the other target moved randomly. In Fig. 5, the horizontal dashed lines represent the reference position of the target. In Fig. 5(a), where the target is stationary, the range bin of the target remains relatively stable over time. However, in Fig. 5(b), due to the presence of RBM, the range bin fluctuates and deviates from the reference position at some moments.

Considering the limitations of the preceding range bin selection method, this paper creatively proposes an adaptive range bin selection method based on phase variance. The method divides all frames into multiple units, and each unit consists of K frames. As the range bin varies slightly over a short period, the range bin selected in the first frame is used for the latter $K-1$ frames within the same unit. The selection process is mainly divided into two stages. In the first stage, the initial range bin is selected based on the energy, and the range bin with the maximum energy is selected. In the second stage, the selection of range bin is based on the phase variance. Considering that, when the human body is relatively static, the range bin changes very little. Hence, in order to reduce the amount of calculation, the subsequent range bin selection only considers range bins near the previously selected range

bin, including a bins before and after it, in a total of $2a + 1$ bins. Additionally, to reduce the influence of interference and noise, the phase changes in the current frame and its vicinity are taken into account. To be specific, the range of frame selection spans b frames before and after the current frame, resulting in a total of $2b + 1$ frames. The steps of the adaptive range bin selection method based on variance are as follows, which can be mainly divided into three steps.

- Starting from the first frame, all frames are divided into multiple units, and every unit is composed of K frames. The K frames in each unit select the same range bin which depends on the bin selected by the first frame in the unit. Suppose U_i represents the ith unit, R_j represents the jth range bin, and F_t represents the tth frame.
- The range bin of all frames in the first unit (U_1) is selected based on energy.

a) In all range bins, the bin R with the maximum energy is regarded as the bin where the human target is located, and select it as the current range bin.

b) The range bin R is not changed in all K frames in U_1.

- The range bin of frames in all units except U_1 is adaptively selected based on phase variance.

a) Take selecting the range bin of the frames in U_i as an example. Suppose that the range bin selected in frames of U_{i-1} is R_j. Then the candidate range bins in frames of U_i is $[R_{j-a}, R_{j+a}]$, a total of $2a + 1$ bins.

b) In U_i, the frame selected for the range bin is $F_{(i-1)K+1}$. Calculate the phase variance of each candidate range bin in the range of $[F_{(i-1)K+1-b}, F_{(i-1)K+1+b}]$, a total of $2b + 1$ frames.

c) The range bin with the maximum variance is selected for all frames in U_i. In each candidate range bin, the phase variance calculation formula is as follows:

$$va_v = \frac{\sum_{u=(i-1)K+1-b}^{u=(i-1)K+1+b} \left(\varphi_u^v - \bar{\varphi}_v\right)^2}{2b+1}, v = j-a, \cdots, j+a \tag{6}$$

where φ_u^v denotes the phase in the vth bin of the uth frame and $\bar{\varphi}_v$ denotes the average value of the phase in the vth bin of frames from $F_{(i-1)K+1-b}$ to $F_{(i-1)K+1+b}$.

This method selects the range bin every K frames, thereby reducing the amount of calculation. Moreover, it considers not only the frame in which the selection is performed, but also a short range of nearby frames, which reduces the impact of interference and noise such as breathing and RBM. Fig. 6 shows the process of selecting the range bin in ith unit. As shown in Fig. 6, the jth range bin where the body is located is selected in the *(i-2)K+1*th frame. Based on this, taking into account the frames indicated by orange lines, the range bin with the maximum phase variance is selected from the candidate range bins within the purple ellipse.

After determining the range bins where the human target is located, the next step is to extract the phase signal from these bins. In this paper, the phase signal is extracted by the arctangent algorithm. To ensure the phase signal remains within $[-\pi, \pi]$ when the displacement $x(t)$ is greater than $\lambda_{\max}/4$, phase unwrapping is then performed on phase signal to obtain the unwrapped signal, which represents the periodic motion of the human thorax in the radar echo signal matrix. This unwrapped signal contains vital signs that are essential for later processing stages.

3) PHASE DIFFERENCE AND IMPULSE NOISE REMOVAL

The phase must be deconvoluted due to a breakpoint issue in the phase derived by the inverse tangent algorithm. The formula for the algorithm is as follows:

$$\phi(n+1) = \begin{cases} \phi(n+1) - 2\pi, \phi(n+1) - \phi(n) > \pi \\ \phi(n+1) + 2\pi, \phi(n+1) - \phi(n) < -\pi \end{cases} \tag{7}$$

To eliminate phase drift and enhance the heartbeat signal which is usually very small and can be easily masked by background noise, the phase difference processing is employed on the unwrapped signal. The process of phase difference is to subtract the previous phase value from the value of the latter phase, and the signal after the processing of phase difference is referred to as phase difference signal.

However, real radar data contain a significant quantity of non-Gaussian noise, such as electromagnetic interference and powerful scattered radar echoes, which can still interfere with the phase difference signal.

In order to further eliminate the non-Gaussian noise and improve the SNR of heartbeat signal, the impulse noise removal processing is then performed during the final signal preprocessing. The resulting signal is referred to as the preprocessing signal. Fig. 7 illustrates the effectiveness of impulse noise removal by comparing the phase difference signal before and after impulse noise removal, i.e., phase difference signal and preprocessing signal. In Fig. 7(a), the amplitude of the impulse noise is almost as high as 3 before removal, indicating a significant interference. However, Fig. 7(b) shows that after impulse noise suppression, the signal impulse noise is significantly reduced, clearly indicating the successful suppression of the impulse noise.

B. MATCHED FILTERING BASED ON SMOOTH SPLINE FITTING

The amplitude of chest vibrations caused by human breathing is significantly greater than that of the heartbeat. Traditional methods attempt to directly filter out the heartbeat signal to eliminate the effect of the breathing signal on heart rate estimation. However, the third and fourth harmonic frequencies of breathing are very close to the heartbeat frequency, which can result in false peaks of breathing harmonics appearing in the heart rate range spectrum [43]. Additionally, unconscious RBM are unavoidable when a person is seating or standing. RBM can reach several millimeters or even tens of centimeters, thus the Doppler spectrum of the heartbeat will be entirely obscured by the signal of broadband noise [44]. To recover the periodicity of the heartbeat signal, previous methods have used polynomial fitting to eliminate motion

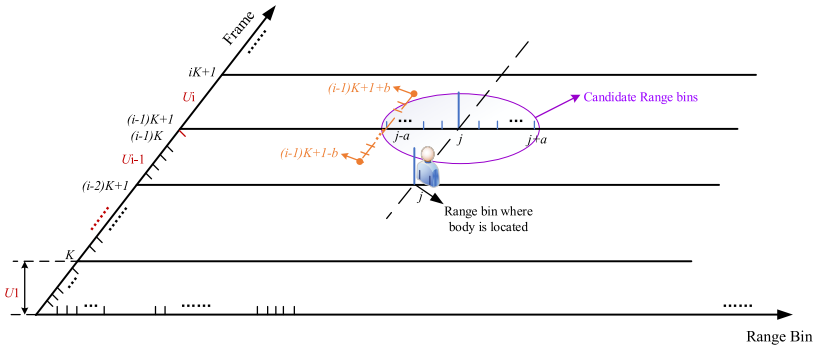

FIGURE 6. Schematic diagram of range bin selection.

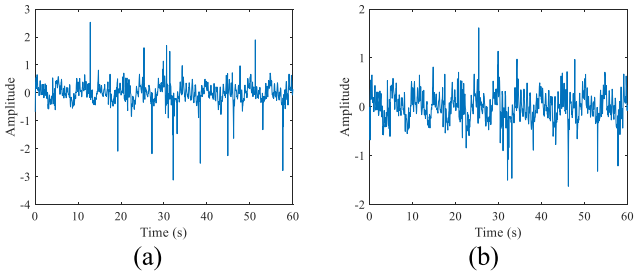

FIGURE 7. Results before and after impulse noise removal: (a) Phase difference signal; (b) Preprocessing signal.

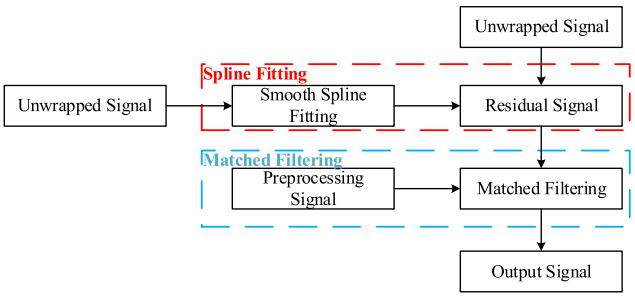

FIGURE 8. Flow chart of the matched filtering based on smooth spline fitting.

[45], but the order of the polynomials must be adapted to the breathing frequency of the human subject [46], which is impractical. In this paper, we employ matched filtering to effectively recover the small-amplitude heartbeat signal in the presence of RBM. To improve the effectiveness of matched filtering, we utilize smooth spline fitting to remove the "burr" in the unwrapped signal and obtain a cleaner template signal. Fig. 8 depicts the matched filtering process flow.

1) SMOOTH SPLINE FITTING

The term "spline curve" refers to a curve generated by a set of control points, and the general shape of the curve is controlled by these points. Depending on whether the curve passes through all the control points or not, splines can be classified as interpolation or approximation splines. For interpolation spline fitting, the fitted curve must pass through all control points; otherwise, it is referred to as approximate spline fitting. In this paper, the latter is employed, and the unwrapped signal serves as the control point.

Compared to heartbeat signals, breathing and RBM have larger distance variations and lower frequencies. In this paper, the phase variations caused by breathing and RBM are estimated through spline fitting.

To remove breathing and RBM with lower frequency and larger distance change compared to the heartbeat signal, the estimation of the phase change caused by breathing and RBM can be fitted by:

$$\min_{\hat{f}} \sum_{n=1}^{N} \left\{\phi(n) - \hat{f}(t_n)\right\}^2 + \lambda \int \hat{f}''(t)^2 dt \tag{8}$$

where $\lambda \geq 0$ is the smoothing parameter, N is the total number of samples, and $\phi(n)$ is the unwrapped signal. The first part of the above equation is used to measure the approximation of the fitted curve to the original phase, and the second part is used to measure the smoothness of the curve, which is the essence of the smoothing spline. $\hat{f}$ is the estimated value of the phase change caused by breathing and RBM, defined as:

$$\hat{f}\,(t) = \sum_{n=1}^{N} \hat{f}(t_n) f_n(t) \tag{9}$$

where $f_n(t)$ are a set of spline basis function. Assume $\hat{\mathbf{P}} = \left[\hat{f}(t_1), \cdots, \hat{f}(t_N)\right]^{\mathrm{T}}$, the roughness loss is of the form [28]:

$$\int \hat{f}''(t)^2 dt = \hat{\mathbf{P}}^{\mathrm{T}} \mathbf{A} \hat{\mathbf{P}} \tag{10}$$

where the elements of $\mathbf{A}$ are $\int f_i''(t) f_j''(t) dt$. We can rewrite (8) as:

$$\min_{\hat{\mathbf{P}}} \left\{\phi - \hat{\mathbf{P}}\right\}^{\mathrm{T}} \left\{\phi - \hat{\mathbf{P}}\right\} + \lambda \hat{\mathbf{P}}^{\mathrm{T}} \mathbf{A} \hat{\mathbf{P}} \tag{11}$$

when $\hat{\mathbf{P}}^* = (\mathbf{I} + \lambda \mathbf{A})^{-1} \phi$, the above equation takes the minimum value, then the estimated phase change caused by breathing and RBM is $\hat{f}(t) = \hat{\mathbf{P}}^{*\mathrm{T}} \mathbf{f}(\mathbf{t})$, where $\mathbf{f}(\mathbf{t})$ is the vector

form of the spline basis function. The residual signal, i.e., the template signal after interference removal, is [29]:

$$h(t) = \phi(t) - \hat{f}(t) \tag{12}$$

where $\phi(t)$ is the unwrapped signal.

2) MATCHED FILTERING

In signal processing, the matched filter is frequently employed to maximize the SNR of a target signal in the presence of noise. It works by convolving the input signal with a template signal that matches the expected characteristics of the target signal. By aligning the input signal with the template signal, the matched filter enhances the recovery of the signal that resembles the template, resulting in a stronger representation of the desired signal and a weaker representation of the noise. This leads to the maximization of the SNR. In this paper, the heartbeat signal hidden in the preprocessing signal is recovered using matched filtering, with the residual signal serving as the template.

The matched filtering result of the vital sign $s(t)$, which is named the output signal, is obtained by convolving the preprocessing signal $y(t)$, which is the conjugate timedomain inversion of the residual signal $h(t)$, expressed in the formula as [47]:

$$s(t) = y(t)h^*(-t) \tag{13}$$

C. VME ALGORITHM

EMD is susceptible to under-envelope, over-envelope, frequency mixing, and endpoint effects. VMD requires specifying the number of mode decompositions in advance [33]; too many modes will result in some false components, while too few will induce mode mixing. Consequently, VME, a simplified version of VMD, has been introduced [48]. The VME algorithm employs the same concepts as the Variational VMD algorithm: Wiener filtering, Hilbert transform, and variational method [49]. By estimating the mode's central frequency, VME extracts eigenmodes with central frequencies close to a predetermined central frequency. This feature avoids the requirement to know the required number of VMD modes. In addition, the computational complexity of extracting certain modes is drastically decreased. Moreover, it effectively solves the problems such as endpoint effects and has been successfully applied in medical and other fields [50]. For these reasons, this paper selects VME to extract the heartbeat signal from the phase signal, i.e., the output signal.

The fundamental premise of VME decomposition of the signal is to solve for the approximation of the mode's center frequency and to extract the eigenmodes with the mode's center frequency as their center frequency. The particular procedures are listed below. 1. The core idea of VME is to construct and solve variational problems, and constrained variational models can be constructed as follows:

$$\begin{cases} f(t) = u_d(t) + f_r(t) \\ \min\limits_{u_d, w_d, f_r} \left\{ \alpha \left\| \partial_t \left[\left(\delta(t) + \frac{j}{\pi t} \right) u_d(t) \right] e^{-jw_d t} \right\|_2^2 \right. \\ \left. + \|\beta(t) f_r(t)\|_2^2 \right\} \end{cases} \tag{14}$$

where $f(t)$ is the input signal; $u_d(t)$ is the desired mode; $f_r(t)$ is the residual noise signal; δ is the Dirac distribution; w_d is the approximate center frequency; α is the quadratic penalty term; and $\beta(t)$ is the impulse response of the filter used.

2. To solve the reconstruction constraint problem, the quadratic penalty term α and the Lagrangian penalty factor λ are introduced to obtain the augmented Lagrangian function as follows:

$$\begin{aligned} L(u_d, w_d, \lambda) = \alpha & \left\| \partial_t \left[\left(\delta(t) + \frac{j}{\pi t} \right) u_d(t) \right] e^{-jw_d t} \right\|_2^2 \\ & + \|\beta(t) f_r(t)\|_2^2 + \|f(t) - (u_d(t) + f_r(t))\|_2^2 \\ & + \left\langle \lambda(t), f(t) - (u_d(t) + f_r(t)) \right\rangle \end{aligned} \tag{15}$$

3. Using the Fourier transform and the alternating direction multiplier algorithm to solve the above variational problem, the alternating update, and can lead to the new expressions as follows:

$$\begin{cases} u_d^{n+1}(w) = \dfrac{f(w) + \alpha^2 \left(w - w_d^{n+1} \right)^4 u_d^n(w) + \frac{\lambda(w)}{2}}{\left[1 + \alpha^2 \left(w - w_d^{n+1} \right)^4 \right] \left[1 + 2\alpha \left(w - w_d^n \right)^2 \right]} \\ w_d^{n+1} = \dfrac{\int_0^\infty w \left| u_d^{n+1}(w) \right|^2 dw}{\int_0^\infty \left| u_d^{n+1}(w) \right|^2 dw} \\ \lambda^{n+1} = \lambda^n + \tau \left[\dfrac{f(w) - u_d^{n+1}(w)}{1 + \alpha^2 \left(w - w_d^{n+1} \right)^4} \right], w \geq 0 \end{cases} \tag{16}$$

where τ is the noise tolerance.

D. SPECTRUM ANALYSIS

In fact, due to the influence of respiratory motion, the extracted phase consists not only of the respiratory and heartbeat components but also the harmonic component of respiration and heartbeat. At this time, the vital signs signal can be expressed as:

$$\begin{aligned} x(t) &= \sum_{m=1}^{M} x_{r_m}(t) + \sum_{n=1}^{N} x_{h_n}(t) \\ &= \sum_{m=1}^{M} A_{r_m} \sin\left(2\pi f_{r_m} t + \phi_{r_m} \right) \\ &\quad + \sum_{n=1}^{N} A_{h_n} \sin\left(2\pi f_{h_n} t + \phi_{h_n} \right) \end{aligned} \tag{17}$$

where $x_{r_1}(t)$ denotes the respiratory component, while $x_{r_m}(t)$ denotes the mth harmonic of respiration, A_{r_m}, f_{r_m}, and ϕ_{r_m} are the corresponding amplitude, frequency, and phase. Similarly, $x_{h_1}(t)$ denotes the heartbeat component, while $x_{h_n}(t)$ denotes the nth harmonic of heartbeat, A_{h_n}, f_{h_n}, and ϕ_{h_n} are

the corresponding amplitude, frequency, and phase. In the process of measuring heartbeat rate, the third and fourth harmonics of respiration are typically very close to the heart rate. Therefore, the resolution and accuracy of frequency measurement must be improved in order to distinguish the heartbeat signal from respiratory harmonics and other unwanted components.

Based on CZT [51], the Double-CZT is proposed in this paper to estimate heart rate in real-time with great precision. The FFT samples at equal intervals on the unit circle in the Z-plane, while the CZT samples at equal angular intervals on any section of the spiral in the Z-plane. Compared with the traditional FFT, which can only obtain a rough spectrum of the entire frequency band, CZT can ignore other frequency bands and only sample in the frequency band of interest, so CZT has a higher resolution with the same number of sampling points.

Sampling at equal angles along a segment of the spiral in the Z-plane, and these sampling points:

$$\begin{aligned} z_k &= AW^{-k} = A_0 e^{j\theta_0} \left(W_0 e^{-j\phi_0}\right)^{-k} \\ &= A_0 e^{j\theta_0} W_0^{-k} e^{jk\phi_0}, k = 0, 1, \cdots, M-1 \end{aligned} \tag{18}$$

where M is the number of sampling points, A_0 is the vector radius of the initial sampling point, θ_0 is the phase of the initial sampling point, ϕ_0 is the angular difference between adjacent sampling points, and W_0 is the elongation of the spiral. The above parameters are determined according to practical requirements. At the fixed point z_k, we convert the recovered phase from $\varphi(n)$ to $\phi(z)$, which is expressed as:

$$\begin{aligned} &\phi(z_k) \\ &= \left(W_0 e^{-j\phi_0}\right)^{\frac{k^2}{2}} \\ &\cdot \sum_{n=0}^{N-1} \left[\varphi(n) \left(A_0 e^{j\theta_0}\right)^{-n} \left(W_0 e^{-j\phi_0}\right)^{\frac{n^2}{2}}\right] \left(W_0 e^{-j\phi_0}\right)^{\frac{-(k-n)^2}{2}} \end{aligned} \tag{19}$$

As can be seen, the starting point z_0 can be chosen arbitrarily, so that CZT can perform high-resolution analysis of the input data from any frequency [52].

In many instances of heart rate measurement, CZT cannot meet the demand of high frequency resolution and measurement accuracy, so we propose the Double-CZT algorithm in this paper [53]. The Double-CZT, which employs CZT twice, determined a peak by using the first CZT, and then the second CZT operation is performed to obtain the final estimated frequency in the frequency range near the peak. The specific process of heart rate estimation with Double-CZT is as follows: Firstly, the CZT is applied to the input signal to attain the frequency spectrum in the human heart rate in $[f_{\min}, f_{\max}]$ Hz, and the frequency at the peak spectrum is used as a rough estimate of the heart rate. The starting point of the refined spectrum analysis is the frequency corresponding to the two spectral intervals on the left side of the first CZT peak spectral line, and the endpoint is the frequency corresponding to the two spectral intervals on the right side of the first CZT peak spectral line. The frequency at the second CZT peak spectrum line is used as the final estimate of heart rate. The specific calculation procedure is as follows. For the first time, N-point CZT is used to process the heartbeat signal with a sampling frequency of f_s, and the frequency resolution is:

$$\Delta f = \frac{f_{\max} - f_{\min}}{N} \tag{20}$$

From here we can see that compared with FFT, CZT can measure frequency in the frequency range we actually care about. For example, in the above heart rate measurement, the sampling frequency is 20 Hz, the frequency resolution of CZT is Δf, while the frequency resolution of FFT at the same number of points is f_s/N. The general range of heart rate is [0.8, 2] Hz, then the frequency resolution of CZT is about 16 times that of FFT.

Considering that the spectral analysis of the signal is implemented on the unit circle, the parameters of the first CZT algorithm are $A_0 = 1$, $W_0 = 1$, $\theta_0 = 2\pi(f_{\max} - f_{\min})/(Nf_s)$, and $\phi_0 = 2\pi f_{\min}/f_s$. Assuming that the spectral line position of the maximum peak obtained after the first CZT is N_1, the frequency scope band range of the second CZT algorithm is $[f_{\min} + (N_1 - 2)\,\Delta f, f_{\min} + (N_1 + 2)\,\Delta f]$. Also, the value of θ_0 can be given:

$$\theta_0 = 2\pi \frac{\Delta f'}{f_s} \tag{21}$$

where $\Delta f'$ is the desired frequency resolution, if it can be achieved after the M-point CZT, then $\Delta f' = 4\Delta f/M$. This can be achieved. Assuming that the spectral line position maximum peak is N_2, the heartbeat rate can be written as:

$$f_{h_1} = f_{\min} + (N_1 - 2)\,\Delta f + N_2 \Delta f' \tag{22}$$

In order to demonstrate the superiority of the Double-CZT algorithm, we conduct a comparison with FFT, MUSIC [54], [55], [56], and the CZT algorithm in terms of measurement accuracy. This comparison is performed by simulating a noise-added sine wave signal.

The experimental parameters are set as follows. The sine wave signal $s(t) = 0.2\sin(2\pi \cdot 1.2t)$ and the signal length is 64. The number of MUSIC antennas is 8, the number of snapshots is 8, and the sampling frequency is 10 Hz. We perform 1000 Monte Carlo simulations of a sine wave signal at each noise level, using the root mean square error (RMSE) as the measurement metric, defined as [57]:

$$RMSE = \sqrt{\frac{1}{N}\sum_{k=1}^{N} (est(k) - true(k))^2} \tag{23}$$

where N is the number of Monte Carlo experiments, $est\,(k)$ and $true\,(k)$ represent the estimated frequency and the true frequency of the sine wave respectively.

The simulation results illustrated in Fig. 9 reveal that the RMSE of FFT consistently exceeds that of MUSIC, CZT, and Double-CZT at any SNR in this experiment. Specifically, the RMSE of FFT is highest when the SNR lies in

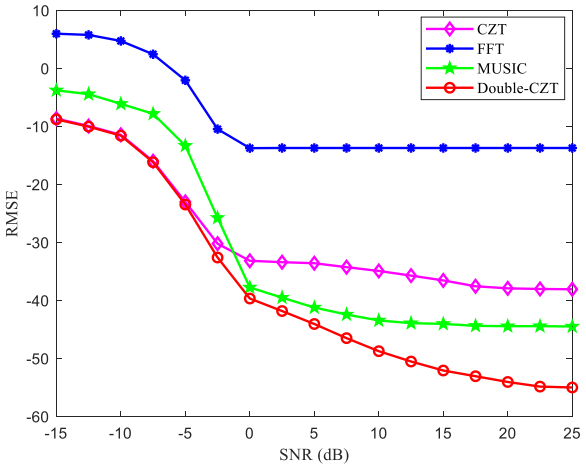

FIGURE 9. RMSEs of frequency estimation among various methods.

[-15, -5] dB. As the SNR increases, the RMSE of FFT gradually decreases, but it still remains significantly higher than that of MUSIC, CZT, and Double-CZT. In the case of MUSIC, the RMSE is greater than that of CZT and Double-CZT when the range of SNR is [-15, -2.5] dB. However, as the SNR increases, the RMSE of MUSIC becomes lower than that of CZT but still higher than that of Double-CZT. For CZT, its RMSE is comparable to that of Double-CZT when the range of SNR is [-15, -5] dB. As the SNR increases, the benefits of Double-CZT become more apparent. In this simulation experiment, the average RMSE values of CZT, FFT, MUSIC, and Double-CZT are 0.081, 0.608, 0.150, and 0.071, respectively. Overall, Double-CZT offers superior frequency measurement accuracy compared to the other three methods.

Moreover, in terms of simulation time, MUSIC requires nearly 20 times longer than CZT and Double-CZT. Although MUSIC has a smaller frequency measurement error than FFT, its real-time implementation is challenging due to its massive computational requirements. This further highlights the advantages of Double-CZT as proposed in this paper, which not only delivers minimal frequency measurement errors and low time consumption but also enables real-time engineering implementation.

V. EXPERIMENTS

In this paper, we conduct experiments using a Texas Instruments mm-Wave AWR 1642 FMCW radar, which operates at 77-81 GHz and has two transmit antennas and four receive antennas, making it a versatile sensor for a variety of applications. To verify our proposed algorithm, we use a DCA 1000 acquisition board to collect data and transfer the data to a computer terminal through a USB interface, and then use MATLAB for simulation and analysis. The configuration parameters of the FMCW radar used in the experiments are listed in Table 1, and their descriptions are depicted in Fig. 10.

Fig. 11 shows the real experiment demonstration, with the subject seated at a distance of approximately 1 m from the

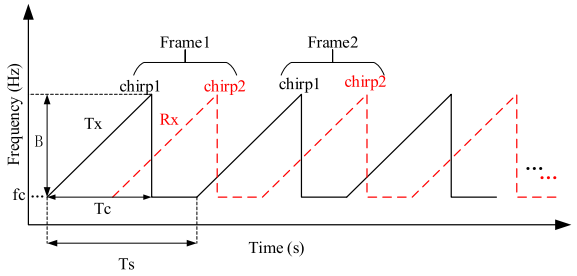

FIGURE 10. The parameter settings of the sensor.

TABLE 1. Radar parameters.

Parameter	Value
Start Frequency, fc	77 GHz
Idle Time, Ti	7 µs
Chirp duration, Tc	50 µs
Frequency Bandwidth, B	3.99 GHz
Frame period, Ts	50 ms
Samples per Chirp	200
Frequency Slope	70 MHz

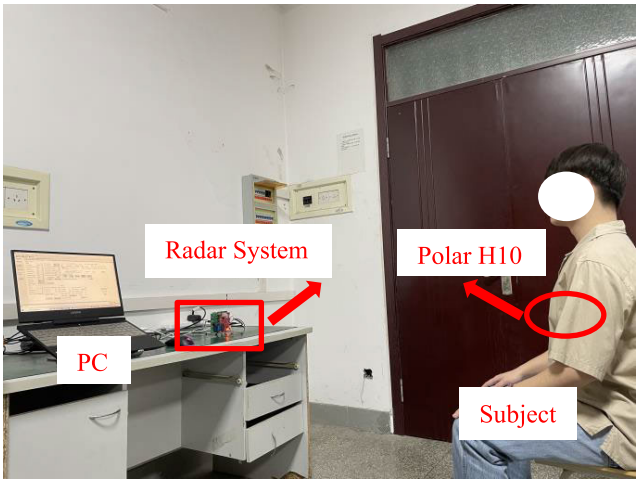

FIGURE 11. Real experiment demonstration.

radar and facing it directly. The subject wore a Polar H10 chest heart rate sensor, which served as a reference for measuring the heartbeat rate. The subject kept their respiratory and heartbeat signs stable before the test, and remained as still as possible during the test, with no other human targets within the sensor's sensing range. Fig. 12 shows the details of the experimental equipment, including the radar system and the chest heart rate sensor.

In order to evaluate the accuracy of heartbeat rate estimation, we use the Polar H10 chest heart rate sensor to measure heart rate as the reference and adopted the mean absolute error (MAE) and mean absolute percentage error (MAPE) as the measurement metric. MAE is defined as [58]:

$$MAE = \frac{1}{N}\sum_{k=1}^{N}(BPM_{\text{est}}(k) - BPM_{\text{true}}(k)) \qquad (24)$$

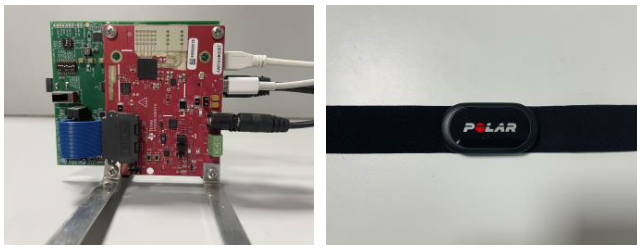

(a) (b)

FIGURE 12. Experimental equipment: (a) AWR 1642 radar system; (b) Polar H10 chest heart rate sensor.

TABLE 2. The parameters settings of VME algorithm.

Parameter	Value
Omega Int	1.2
Penalty Factor	1000
Tolerance to Noise	0
Tolerance of Convergence Criterion	1e-7
Data Fidelity Balance Parameters	20000

MAPE is defined as [11]:

$$MAPE = \frac{1}{N}\sum_{k=1}^{N}\frac{(BPM_{\text{est}}(k) - BPM_{\text{true}}(k))}{BPM_{\text{true}}(k)} \tag{25}$$

where N denotes the total number of time windows within the observation time for each data set, $BPM_{\text{true}}(k)$ and $BPM_{\text{est}}(k)$ are the true heart rate measured by the Polar H10 chest heart rate sensor and the estimated heart rate obtained by the algorithm at the kth time window.

We collect signals from 1200 frames, the slow time sampling frequency is 20 Hz, and use VME to extract heartbeat signal. According to a large number of simulation experiments, Table 2 gives the optimal parameters of VME algorithm.

VI. RESULTS

A. ANALYSIS OF ADAPTIVE RANGE BIN SELECTION AND MATCHED FILTERING BASED ON SMOOTH SPLINE FITTING

1) ADAPTIVE RANGE BIN SELECTION

Let $K = 128$, $a = 5$, $b = 5$ mentioned in Section IV, and then the spectrum of the extracted phase from the selected range bins is shown in Fig. 13. The blue dashed line represents the original energy-based range bin selection method, and the red solid line represents the adaptive range bin selection method proposed in this paper. It should be illustrated that the reference heartbeat rate given by the Polar H10 chest heart rate sensor is 79 beat per minute (bpm), which corresponds to a signal frequency of 1.316 Hz. We can observe from Fig. 13 that the peak frequency of the red line (proposed method) is 1.317 Hz. On the other hand, the peak in the blue line is shifted, and the real heartbeat is obscured by the unwanted signals. Therefore, the range bins selected using the proposed method contain more heartbeat information with less interference.

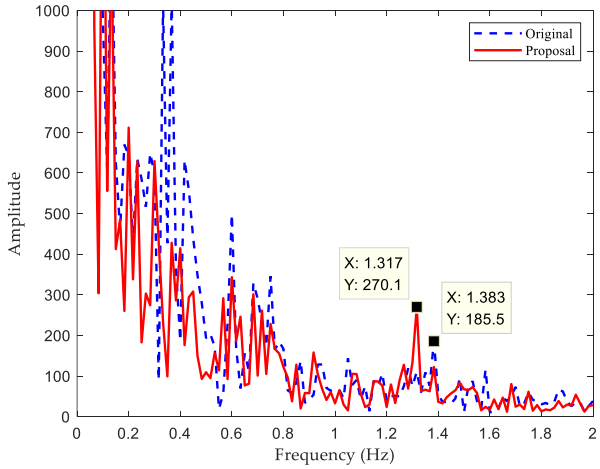

FIGURE 13. Spectrogram of the phase signals from the range bins selected by the original method and proposed method.

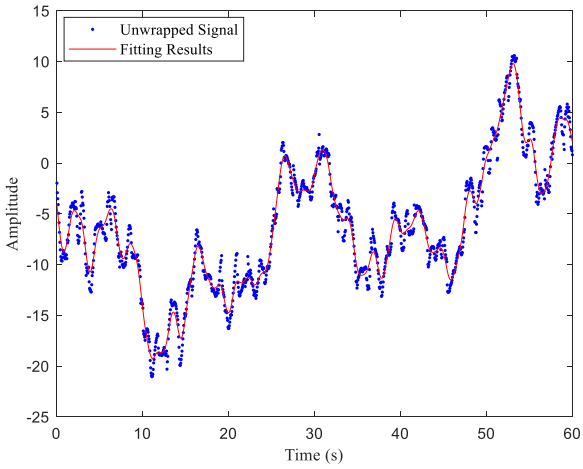

FIGURE 14. Unwrapped signal and fitting results.

2) SMOOTH SPLINE FITTING

The results after fitting the unwrapped signal are shown in Fig. 14. The blue dots represent the original unwrapped signal and the red solid line shows the fitting results corresponding to the breathing effect and RBM.

The residual signal is obtained by subtracting the fitting results from the unwrapped signal. Fig. 15(a) shows the preprocessing signal, which is the signal after impulse noise removal shown in Fig. 2, and Fig. 15(b) shows the residual signal. It can be seen from Fig. 15(a), the preprocessing signal has no obvious periodicity, and its amplitude varies from -1.6 rad to 1.2 rad, which is due to the impact of breathing and RBM. On the contrary, the amplitude of residual signal does not exceed 0.8 in Fig. 15(b). In addition, the residual signal exhibits a distinct prototype of the heartbeat signal and demonstrates periodicity associated with the heartbeat.

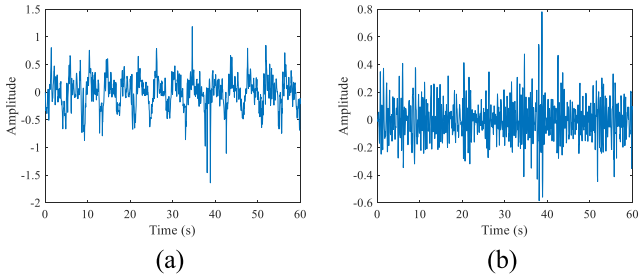

FIGURE 15. Waveform of the preprocessing signal and the residual signal in the time domain: (a) The preprocessing signal; (b) The residual signal.

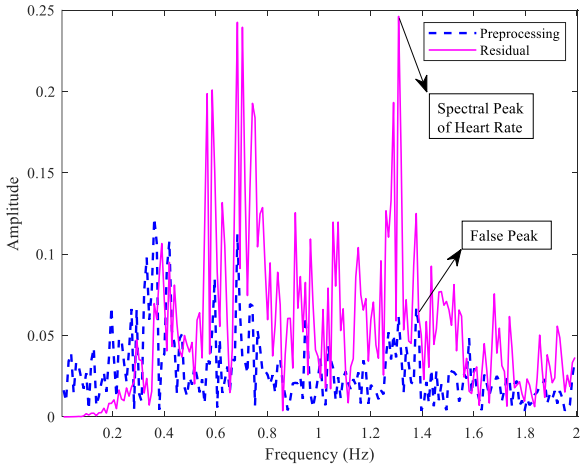

FIGURE 16. Spectrogram of the preprocessing signal and residual signal.

FFT is performed on both the original preprocessing signal and the residual signal respectively, and their frequency spectrums are shown in Fig. 16. The blue dashed line in Fig. 16 represents the spectrum of the original preprocessing signal, and the purple line represents the spectrum of the residual signal. The subject's heart rate, measured by the Polar H10 chest heart rate sensor, is 79 bpm, corresponding to a real heart rate value of approximately 1.32 Hz. It can be seen that the heartbeat signal in the original preprocessing signal is drowned in noise and interference, making it difficult to extract. Nevertheless, after applying smooth spline fitting to obtain the residual signal, the lower frequency range, where respiration occurs, is attenuated. Moreover, the prominent peaks in the residual signal closely resemble the real heartbeat frequency measured by the reference sensor. Apparently, by using smooth spline fitting, the residual signal can exhibit a characteristic of the heartbeat signal to a large extent. Consequently, a matched filter can be designed by taking the residual signal as the template.

3) MATCHED FILTERING

Using the residual signal as a template, a matched filter can be built and implemented by taking the preprocessing signal as input. The spectrum of the output signal of the matched filter is shown in Fig. 17. Notably, the primary peak of the heartbeat signal is more prominent, while the spurious peaks generated

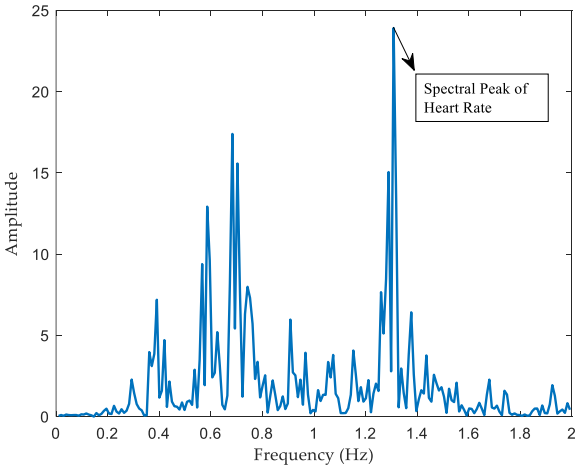

FIGURE 17. Spectrogram of the output signal of the matched filter.

by other effects such as respiratory harmonic, RBM, and other interference have been effectively eliminated. To assess the efficiency of the matched filtering approach, we performed 1000 simulations and calculated the average runtime. The average runtime is 0.158 milliseconds, which indicates that matched filtering can be implemented in real-time. It should be noted that experiments were done in a PC with Intel (R) Core (TM) i7-1065G7 CPU @ 1.30GHz 1.50GHz.

To further analyze the effect of the matched filtering, we use the SNR in the frequency domain for quantitative analysis. Assuming that the spectral peak in 0.8-2 Hz corresponds to a spectral line position of N_0, its SNR can be expressed as:

$$SNR = 10\lg\left(\frac{sum\left(\sum_{i=-5}^{5} S^2\left(N_0 - i\right)\right)}{S^2(f) - sum\left(\sum_{i=-5}^{5} S^2\left(N_0 - i\right)\right)}\right) \tag{26}$$

where $S^2(f)$ denotes the total energy of the spectrum and $S^2(N_0)$ denotes the energy at the peak of the signal spectrum. Taking Fig. 16 and Fig. 17 as an example, the SNR of the preprocessing signal, the residual signal, and the output signal of the matched filter are -17.78 dB, -11.01 dB, and -6.28 dB, respectively. This indicates that there is an SNR improvement of 6.77 dB by adopting the smooth spline fitting. Furthermore, an additional improvement of 4.73 dB is achieved by employing the matched filtering. Consequently, remarkable performance improvement in heartbeat rate measurement can be achieved by adopting the method of matched filtering based on smooth spline fitting.

In order to further verify the effectiveness of range bin selection and matched filtering based on smooth spline fitting method proposed in this paper, we analyze the heartbeat signal extracted by VME for the following three schemes. Scheme 1: The range bin is selected by the original energy-based method, and the preprocessing signal is the VME input signal. In addition, FFT is chosen as the method for heart rate estimation. Scheme 2: Different from scheme 1, the range bin

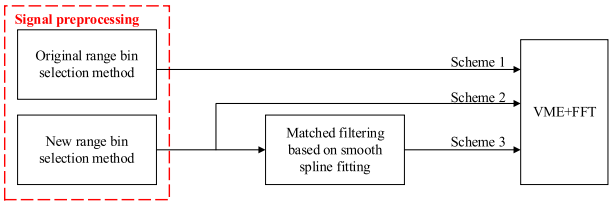

FIGURE 18. Brief flow diagram of various schemes.

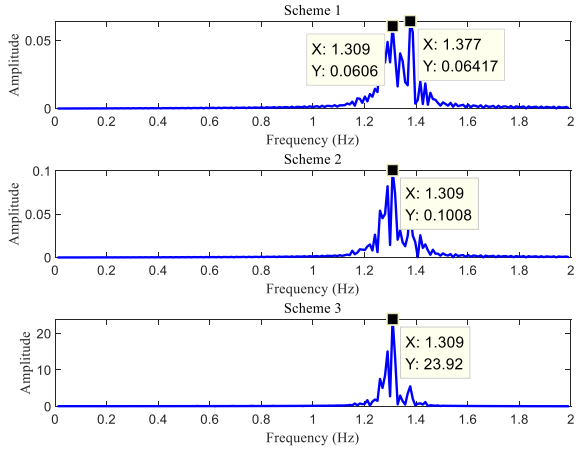

FIGURE 19. Spectrogram of heartbeat signals obtained by VME.

selection method is the adaptive range bin selection method. Scheme 3: Different from scheme 2, the method of matched filtering based on smooth spline fitting is adopted. The brief flow diagram of these schemes is shown in Fig. 18, which more clearly shows the differences among the three schemes.

Fig. 19 shows the spectrum of output signal for scheme 1, scheme 2, and scheme 3, respectively. It can be seen that the heartbeat signal obtained by scheme 1 contains more clutter (respiratory harmonics, cross-tuned signals, heterodyne waves from RBM, and other unwanted signals), and the peaks are not obvious, even a false peak appears. Due to the fact that the heart rate reference value detected by the Polar H10 chest heart rate sensor is 79 bpm, the peak value of the real heartbeat signal should be in the vicinity of 1.3 Hz. Scheme 1 yields a spectrogram with the largest peak at 1.377 Hz, i.e., a false peak, which will increase the measurement error for the final heart rate. Scheme 2 shows the proper peak and a cleaner spectrogram. Consequently, the range bin selection method proposed in this paper is preferable. Additionally, scheme 3 effectively suppresses the clutter, resulting in a clear observation of the peak in the heartbeat signal. Comparing scheme 2 and scheme 3, it is evident that scheme 3 yields a purer spectrum with a more pronounced peak. This highlights the advantages of matched filtering based on smooth spline fitting.

B. HEART RATE MEASUREMENT ANALYSIS

In each experiment, subjects were examined for one minute, and 60 continuous heart rate reference values were gathered via the Polar H10 chest heart rate sensor. During each experiment, the sliding window length and the sliding step length were set as 512 and 20 [59], respectively, and data to be processed slides once every second starting from 26 s. As a result, 35 continuous heart rate values were obtained. To illustrate the effectiveness of the proposed algorithms, we analyze the MAE of the heart rate estimated by various schemes.

TABLE 3. MAE of heart rate by different schemes (MAE units: bpm).

Subject	Scheme 1	Scheme 4	Scheme 5
1	2.6	2.171	1.6
2	8.428	3.6	2.971
3	0.828	0.828	0.742
4	2	1.942	0.914
5	2.342	2.142	1.914
Average	3.239	2.136	1.628

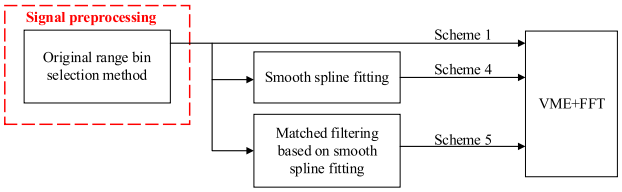

FIGURE 20. Brief flow diagram of various schemes.

1) PERFORMANCE IMPROVEMENT BY USING MATCHED FILTERING BASED ON SMOOTH FITTING

To exhibit the validity of the smooth spline fitting and the matched filtering based on smooth spline fitting, we compare and analyze the MAE of scheme 1, scheme 4, and scheme 5. Scheme 4: Different from scheme 1, the input signal of VME is a residual signal. Scheme 5: Different from scheme 4, the input signal of VME is the output signal of the matched filter. We use the MAE obtained from scheme 1, scheme 4, and scheme 5 to demonstrate the effect of fitting and matching respectively. The brief flow diagram of these schemes is shown in Fig. 20. Table 3 exhibits the MAE of scheme 1, scheme 4, and scheme 5, respectively. The average MAEs of heart rate obtained by three schemes mentioned above are 3.239 bpm, 2.136 bpm, and 1.628 bpm, respectively. The results show that the average MAE is reduced from 3.239 bpm to 2.136 bpm by using smooth spline fitting. Moreover, based on smooth spline fitting, the average MAE can be further decreased to 1.628 bpm by adopting matched fitting.

We have verified the effectiveness of the method of matched filtering based on spline fitting from three aspects: SNR, the spectrum of the heartbeat signal, and the MAE of heart rate. To be specific, the SNR of the output signal of the matched filter is improved, the spectrum of the heartbeat signal extracted by VME is cleaner, and the heart rate measurement error is smaller under the same conditions. It can be concluded that estimation accuracy can be improved significantly by using smooth spline fitting, and remarkable

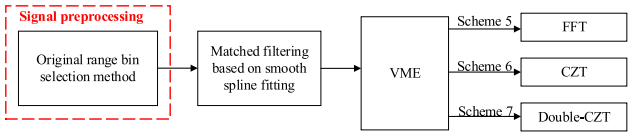

FIGURE 21. Brief flow diagram of various schemes.

TABLE 4. MAE of heart rate by different frequency measurement methods (MAE units: bpm).

Subject	Scheme 5	Scheme 6	Scheme 7
1	2.6	1.057	0.742
2	1.828	0.711	0.514
3	1.057	1.028	0.6
4	1.571	0.542	0.485
5	2.428	1.542	1.085
Average	1.896	0.976	0.685

improvement can be further attained by adopting matched filtering on the basis of smooth spline fitting.

2) PERFORMANCE IMPROVEMENT BY USING DOUBLE-CZT

Scheme 6: Different from scheme 5, CZT is selected as the heart rate estimation method. Scheme 7: Different from scheme 5, Double-CZT proposed in this paper is selected as the heart rate estimation method. We prove the superiority of Double-CZT in heart rate estimation from the MAE obtained by scheme 5, scheme 6, and scheme 7. The brief flow diagram of the schemes is shown in Fig. 21. Table 4 exhibits the MAE of scheme 5, scheme 6, and scheme 7, respectively.

According to Table 4, the average MAEs of heart rate obtained by three schemes mentioned above are 1.896 bpm, 0.976 bpm, and 0.685 bpm, respectively. The results show that the average MAE is reduced from 1.896 bpm to 0.976 bpm by using CZT. Moreover, the average MAE can be further decreased to 0.685 bpm by adopting Double-CZT. In short, Double-CZT outperforms FFT and CZT in heart rate estimation. To provide a visual comparison of the different frequency measurement methods, we selected a set of representative data from Table 4 for analysis. The resulting curves of heart rate versus time are presented in Fig. 22. It can be seen that the heart rate estimate by Double-CZT frequency measurement closely follows the reference value, effectively reflecting the current heart rate fluctuations. Conversely, FFT exhibits significant deviations from the reference heart rate value in the 25th-35th sliding windows, and CZT shows notable deviations in the 5th-7th and 29th-32th sliding windows.

3) PERFORMANCE IMPROVEMENT BY ADOPTING ADAPTIVE RANGE BIN SELECTION

Scheme 8: Differs from scheme 7 in that it employs the adaptive range bin selection method. We demonstrate the effectiveness of the proposed method by comparing the MAE obtained by scheme 7 and scheme 8. The brief flow diagram

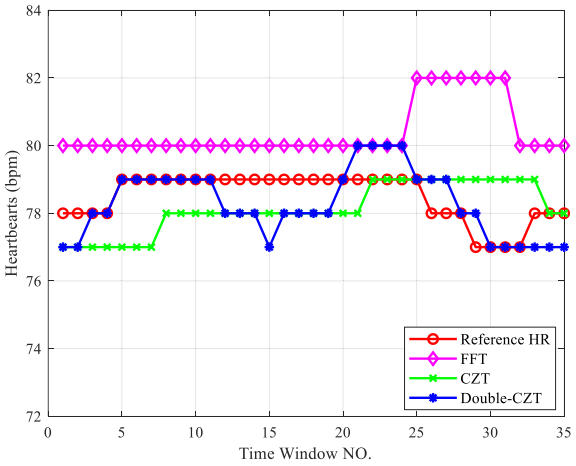

FIGURE 22. Heart rate curves under different frequency measurement methods.

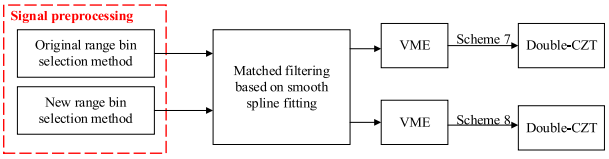

FIGURE 23. Brief flow diagram of various schemes.

TABLE 5. MAE of heart rate by different range bin selection methods (MAE units: bpm).

Subject	Scheme 7	Scheme 8
1	3.142	0.6
2	1.057	0.711
3	1.342	0.828
4	0.714	0.457
5	3.142	1.714
Average	1.879	0.862

of the schemes is shown in Fig. 23, and Table 5 presents the MAE value of both schemes.

The results presented in Table 5 highlight the significant impact of the adaptive range bin selection method on the accuracy of heart rate estimation. Scheme 8, which uses the proposed method, achieves an average MAE of 0.862 bpm, while scheme 7, which uses the traditional range bin selection method, has an average MAE of 1.879 bpm. This demonstrates that the adaptive range bin selection method can improve the accuracy of heart rate estimation by approximately 1 bpm under the same conditions. Furthermore, Table 5 demonstrates that the MAE of scheme 7 is as high as 3 bpm. This finding shows that the traditional range bin selection method fails to correctly select the bins where the human body is located. As a result, the VME algorithm cannot extract the heartbeat signal effectively, leading to a significant discrepancy between the estimated heart rate and the reference heart rate.

TABLE 6. Estimation results of heart rate under different schemes.

Subject	Gender	BMI	Ref. [11]		Ref. [16]		Ref. [24]		Ref. [28]		Ref. [37]		Our Work	
			MAE (bpm)	MAPE (%)	MAE (bpm)	MAPE (%)	MAE (bpm)	MAPE (%)	MAE (bpm)	MAPE (%)	MAE (bpm)	MAPE (%)	MAE (bpm)	MAPE (%)
1	Male	22.8	2.371	3.2	3.285	4.45	2.485	3.39	1.371	1.87	0.685	0.93	0.285	0.39
2	Male	20.1	7.542	12.97	3.314	5.69	2.942	5.02	7.885	13.36	7.857	13.45	1.8	4.24
3	Male	24	24.114	34	7.085	10	3.485	4.92	2.885	4.07	1.628	2.29	0.828	1.16
4	Male	25.6	8.257	10.26	2.542	3.17	2.457	3.06	1	1.25	0.657	0.82	0.628	0.78
5	Male	21.7	6.6	7.77	1.314	1.55	5.257	6.21	3.8	4.48	0.914	1.08	0.886	0.85
6	Female	20.3	11.057	13.56	5.914	7.3	6.428	7.96	2.514	3.1	2.428	3.02	0.8	0.98
7	Female	21	2.8	3.85	4.542	6.21	2.914	3.99	2.057	2.81	1	1.37	0.685	0.9
8	Female	23.2	2.457	3.12	2.6	3.28	2.6	3.28	0.714	0.86	0.914	0.93	0.714	0.43
9	Female	19.8	2.971	4.24	5.085	8.1	19.171	30.39	4.058	7.73	4.142	6.59	0.885	0.99
10	Female	18.7	1.485	1.87	4.714	5.8	9.657	12.06	1.657	2.07	7.657	9.56	0.714	0.89
Average			6.965	9.484	4.039	5.555	5.739	8.028	2.794	4.16	2.788	4.004	0.822	1.161
Standard Deviation			6.463	9.113	1.656	2.406	4.985	7.895	2	3.597	2.681	4.185	0.365	1.051

Based on the discussions presented in Section VI, it can be concluded that the adaptive range bin selection method can make the spectrum of the heartbeat signal cleaner and improve the heart rate estimation accuracy. In short, we illustrate the effectiveness of the range bin selection method proposed in this paper from the perspectives of the spectrum of heartbeat signal and MAE of heart rate.

C. PERFORMANCE ANALYSIS OF THE WHOLE SCHEME PROPOSED

In this section, we conducted a comprehensive analysis of the proposed scheme. Firstly, we compared the estimated heart rate of each subject at each moment with the reference heart rate. Secondly, we compared the heart rate estimation results of our scheme with existing works, including results from actual simulations and reported. This comparison involved metrics such as MAE and the standard deviation (SD). Through these comparisons and evaluations, we emphasized the superiority and contribution of our proposed scheme.

1) ANALYSIS OF HEART RATE ESTIMATION RESULTS OF OUR WORK FOR EACH SUBJECT

Fig. 24 exhibits a bar graph illustrating the average estimated heart rate using our proposed scheme for ten subjects, and the average reference heart rate is represented by a pentagram. The error bar in Fig. 24 refers to the maximum deviation between the estimated and reference heart rate for each subject. It can be observed that the average estimated heart rate of the subjects closely aligns with the average reference heart rate, and the deviation at each moment is minimal. These findings affirm the effectiveness of our scheme in accurately capturing the trends of real heart rate fluctuations.

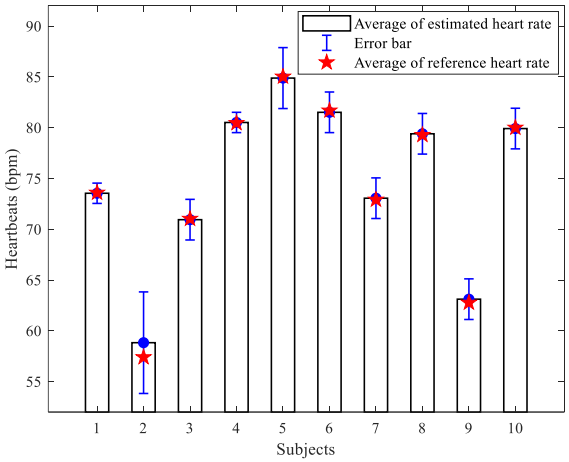

FIGURE 24. Average of estimated heart rate using the proposed scheme versus that of the reference.

2) COMPARISON OF HEART RATE ESTIMATION RESULTS FROM DIFFERENT SCHEMES FOR EACH SUBJECT

To show the superiority of our proposed scheme, we mainly compare the performance of the proposed scheme 8 with the existing classical works. Tests were conducted on a randomly selected group of ten subjects. It is important to note that, in order to demonstrate the universality of the proposed scheme, we split the data for validation and test. The validation data from our database was used to verify the effectiveness of the proposed algorithms split-step as mentioned above. The test data was used to compare the whole scheme with existing schemes. The results are shown in Table 6. It can be seen that the average MAEs of [11], [16], [24], [28], and [37] and our work are 6.965 bpm, 4.039 bpm, 5.739 bpm, 2.794 bpm, 2.788 bpm, and 0.822 bpm, respectively. Obviously, significant improvement in the estimation accuracy

TABLE 7. Comparison of the proposed with the other existing works.

Ref.	Radar	Range (m)	Error of heart rate (%)
[4]	FMCW	0.5	3.02
[5]	CW	0.5-1.5	3.5
[38]	FMCW	0.6-0.8	4.19-6.95
[41]	FMCW	1.7	20
[60]	FMCW	0.28-0.7	2.925
[61]	FMCW	0-5	3.85
[62]	FMCW	1.4	2.4
Our Work	FMCW	1	1.161

of heart rate can be achieved by adopting our scheme. Furthermore, the stability of each scheme was assessed by calculating the SD of MAEs for the ten subjects, as shown in Table 7. The SD values for [11], [16], [24], [28], and [37] and our work are 6.463, 1.656, 4.985, 2, 2.681, and 0.365, respectively. Specifically, the MAE of our work ranges from 0.285 bpm to 1.8 bpm, indicating only a slight variation in estimation accuracy for each subject. In contrast, in other works such as [11], the MAE for the ten subjects ranges from 1.485 bpm to 24.114 bpm, and the MAE of [24] ranges from 2.457 bpm to 19.171 bpm. This result demonstrates that our proposed scheme is less affected by user heterogeneity, and have excellent stability and reliability. The MAPE for each group of experiments is also presented in Table 6, further highlighting the superior performance of the proposed scheme in terms of both the average and SD of MAPEs. In summary, the proposed scheme has high accuracy and good algorithm stability under the same conditions after numerous experiments. Therefore, the proposed scheme has great potential for practical applications.

3) COMPARISON OF OUR RESULTS WITH EXISTING WORKS REPORTED

According to the heart rate estimation errors reported in studies, another comparison results with several existing works based on radar system are summarized in Table 7. It can be found that our proposed work exhibits higher accuracy in heart rate detection.

D. EFFECTS OF DISTANCE AND ORIENTATION

This section focuses on investigating the impact of the distance and orientation between the FMCW radar and the subject on the accuracy of heart rate estimation. Fig. 25(a) and (b) illustrate two different setups, one with subjects seated face-to-face and the other with subjects seated back-to-back with the radar. The subjects were monitored at five locations within a range of 0.5 m to 2.5 m from the radar. Table 8 shows the MAE and MAPE for one subject, and Fig. 26(a) displays the distribution of MAEs at different distances when the subject was seated facing the radar. Similarly, Fig. 26(b) presents the MAE distribution at different distances when the subject was seated with their back against the radar. The pentagrams in Fig. 26 represent the average MAEs. It can be

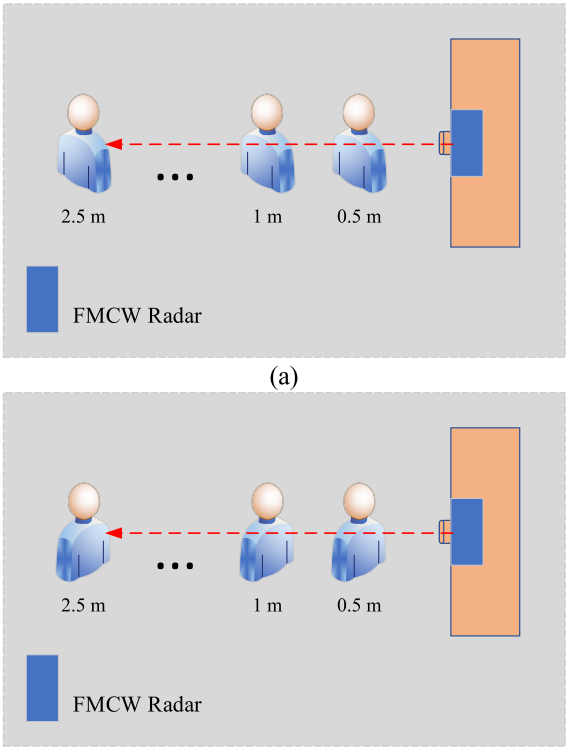

FIGURE 25. Experimental setup: (a) The subjects were seated face-to-face with the radar at different distances; (b) The subjects were seated back-to-back with the radar at different distances.

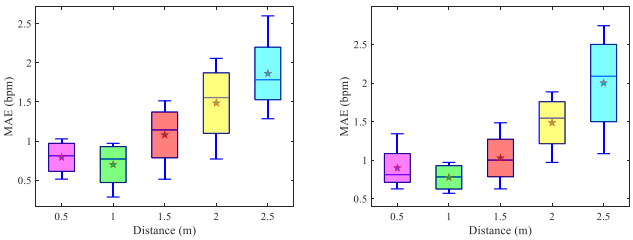

FIGURE 26. Distribution of MAEs at different distances and orientations: (a) The subjects were seated face-to-face with the radar at different distances; (b) The subjects were seated back-to-back with the radar at different distances.

observed that the heart rate estimation accuracy can reach 98% within a range of 1.5 m, as the distance increases to 2.5 m, the estimation accuracy gradually decreases but still achieves 96.5%. Extensive experiments demonstrate that the optimal distance for accurate estimation of the heart rate is 1 m. Furthermore, it can be concluded that the accuracy of heart rate estimation is similar for both facing and backing scenarios. Therefore, in practical applications, the choice of performing heart rate detection from the front or back can be based on specific requirements.

E. EFFECTS OF ANGLES

This section investigates the influence of the angle between the radar's transmission antenna directional vector and the subject on the accuracy of heart rate estimation. Fig. 27 shows the subjects were seated at angles of 0°, 15°, and 30° with

TABLE 8. Heart rate estimation results for different distances and orientations.

Distance (m)	Orientation	MAE (bpm)	MAPE (%)
0.5	Front	0.885	1.25
	Back	0.942	1.33
1	Front	0.714	0.89
	Back	0.682	0.97
1.5	Front	1.057	1.54
	Back	1.285	1.67
2	Front	1.885	2.52
	Back	1.628	2.18
2.5	Front	2.257	3.44
	Back	2.6	3.37

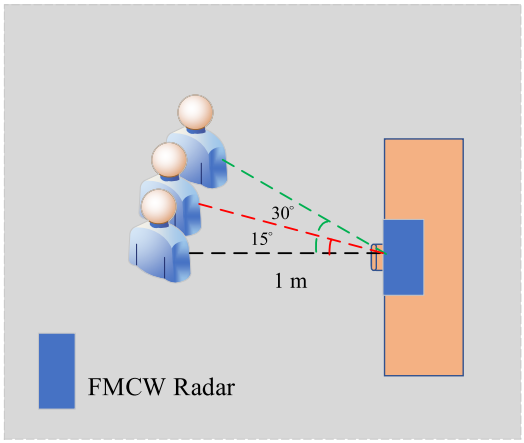

FIGURE 27. Experimental setup: The subjects were seated at different angles with a distance of 1 m from the radar.

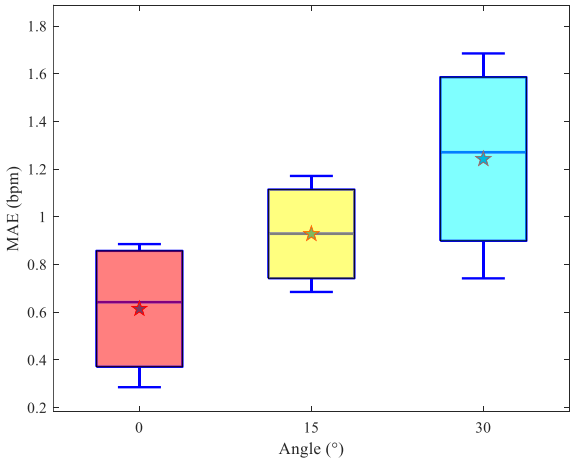

FIGURE 28. Distribution of MAEs when the subjects were seated at different angles with a distance of 1 m from the radar.

respect to the radar, at a distance of 1 m. Table 9 presents the MAE and MAPE for one subject. The distribution of MAEs at different angles is depicted in Fig. 28, with the pentagrams representing the average MAEs. To be specific, the average MAEs at 0°, 15°, and 30° are 0.614 bpm, 0.928 bpm, and 1.242 bpm, respectively. Apparently, the average MAE

TABLE 9. Heart rate estimation results for different angles.

Angle (°)	Distance (m)	MAE (bpm)	MAPE (%)
0	1	0.571	0.76
15	1	0.914	1.23
30	1	1.657	2.22

gradually increases as the angle increases. This result can be attributed to the decrease in antenna gain. However, the error of our work remains acceptable within the radar's 60° viewing angle range.

VII. CONCLUSION

In this paper, a new scheme for heart rate detection is proposed, which consists of three new signal processing methods. Firstly, the adaptive range bin selection method is proposed taking the phase change in multiple frames into consideration. Therefore, the range bins containing phase information of vital signs can be found in the presence of RBM, which is validated from two facets of frequency spectrum analysis and estimation accuracy of heartbeat rate. Secondly, we adopt smooth spline fitting and matched filtering to suppress interference and noise. Experiment results and theoretical analysis demonstrate that SNR of the heartbeat signal can be greatly improved and an accuracy heart rate estimation can be achieved. It is worth mentioning that the method has low computation burden and less running time. Finally, Double-CZT is proposed for improving the performance of spectrum analysis, and simulation results show that high estimation accuracy of frequency can be achieved. Extensive experiments are done to analyze performance of the new scheme. The average MAE of the heartbeat rate is less than 0.9 bpm, also MAEs vary slightly in different experiments, and the standard deviation is 0.365, which indicate the proposed scheme can achieve high precision and stable heart rate detection. Compared to traditional schemes, the estimation accuracy of heartbeat rate can be greatly improved. Overall, the proposed scheme has very good performance in heartbeat rate estimation and considerable potential in real-time heart rate detection.

REFERENCES

[1] Y. Han, T. Lauteslager, T. S. Lande, and T. G. Constandinou, "UWB radar for non-contact heart rate variability monitoring and mental state classification," in *Proc. 41st Annu. Int. Conf. IEEE Eng. Med. Biol. Soc. (EMBC)*, Berlin, Germany, Jul. 2019, pp. 6578–6582.

[2] U. R. Acharya, K. P. Joseph, N. Kannathal, C. M. Lim, and J. S. Suri, "Heart rate variability: A review," *Med. Biol. Eng. Comput.*, vol. 44, no. 12, pp. 1031–1051, Nov. 2006.

[3] K. Fujiwara, E. Abe, K. Kamata, C. Nakayama, Y. Suzuki, T. Yamakawa, T. Hiraoka, M. Kano, Y. Sumi, F. Masuda, M. Matsuo, and H. Kadotani, "Heart rate variability-based driver drowsiness detection and its validation with EEG," *IEEE Trans. Biomed. Eng.*, vol. 66, no. 6, pp. 1769–1778, Jun. 2019.

[4] S. Ji, H. Wen, J. Wu, Z. Zhang, and K. Zhao, "Systematic heartbeat monitoring using a FMCW mm-wave radar," in *Proc. IEEE Int. Conf. Consum. Electron. Comput. Eng. (ICCECE)*, Guangzhou, China, Jan. 2021, pp. 714–718.

[5] Y. Ding, X. Yu, C. Lei, Y. Sun, X. Xu, and J. Zhang, "A novel real-time human heart rate estimation method for noncontact vital sign radar detection," *IEEE Access*, vol. 8, pp. 88689–88699, 2020.

[6] Z. Gao, L. Ali, C. Wang, R. Liu, C. Wang, C Qian, H. Sung, and F. Meng, "Real-time non-contact millimeter wave radar-based vital sign detection," *Sensors*, vol. 22, no. 19, p. 7560, 2022.

[7] K.-M. Chen, Y. Huang, J. Zhang, and A. Norman, "Microwave life-detection systems for searching human subjects under earthquake rubble or behind barrier," *IEEE Trans. Biomed. Eng.*, vol. 47, no. 1, pp. 105–114, Jan. 2000.

[8] S. Hu, R. L. Bowlds, Y. Gu, and X. Yu, "Pulse wave sensor for non-intrusive driver's drowsiness detection," in *Proc. Annu. Int. Conf. IEEE Eng. Med. Biol. Soc.*, Minneapolis, MN, USA, Sep. 2009, pp. 2312–2315.

[9] K. Lee, D. K. Han, and H. Ko, "Video analytic based health monitoring for driver in moving vehicle by extracting effective heart rate inducing features," *J. Adv. Transp.*, vol. 2018, Dec. 2018, Art. no. 8513487.

[10] K. J. R. Liu and B. Wang, *Wireless AI: Wireless Sensing, Positioning, IoT, and Communications*. Cambridge, U.K.: Cambridge Univ. Press, 2019.

[11] Z. Ling, W. Zhou, Y. Ren, J. Wang, and L. Guo, "Non-contact heart rate monitoring based on millimeter wave radar," *IEEE Access*, vol. 10, pp. 74033–74044, 2022.

[12] G. Wang, C. Gu, T. Inoue, and C. Li, "A hybrid FMCW-interferometry radar for indoor precise positioning and versatile life activity monitoring," *IEEE Trans. Microw. Theory Techn.*, vol. 62, no. 11, pp. 2812–2822, Nov. 2014.

[13] G. Wang, J.-M. Muñoz-Ferreras, C. Gu, C. Li, and R. Gómez-García, "Application of linear-frequency-modulated continuous-wave (LFMCW) radars for tracking of vital signs," *IEEE Trans. Microw. Theory Techn.*, vol. 62, no. 6, pp. 1387–1399, Jun. 2014.

[14] D. Zhang, M. Kurata, and T. Inaba, "FMCW radar for small displacement detection of vital signal using projection matrix method," *Int. J. Antennas Propag.*, vol. 2013, Dec. 2013, Art. no. 571986.

[15] Y. Xiong, S. Chen, X. Dong, Z. Peng, and W. Zhang, "Accurate measurement in Doppler radar vital sign detection based on parameterized demodulation," *IEEE Trans. Microw. Theory Techn.*, vol. 65, no. 11, pp. 4483–4492, Nov. 2017.

[16] *mmWave Vital Signs Lab*. Accessed: Apr. 16, 2021. [Online]. Available: https://training.ti.com/mmWave-vital-signs-lab

[17] P. Zhao, C. X. Lu, B. Wang, C. Chen, L. Xie, M. Wang, N. Trigoni, and A. Markham, "Heart rate sensing with a robot mounted mmWave radar," in *Proc. IEEE Int. Conf. Robot. Autom. (ICRA)*, May 2020, pp. 2812–2818.

[18] A. Danzer, T. Griebel, M. Bach, and K. Dietmayer, "2D car detection in radar data with PointNets," in *Proc. IEEE Intell. Transp. Syst. Conf. (ITSC)*, Oct. 2019, pp. 61–66.

[19] A. D. Singh, S. S. Sandha, L. Garcia, and M. Srivastava, "RadHAR: Human activity recognition from point clouds generated through a millimeter-wave radar," in *Proc. 3rd ACM Workshop Millimeter-Wave Netw. Sens. Syst.*, 2019, pp. 51–56.

[20] S. An and U. Y. Ogras, "MARS: mmWave-based assistive rehabilitation system for smart healthcare," *ACM Trans. Embedded Comput. Syst. (TECS)*, vol. 20, no. 5s, pp. 1–22, 2021.

[21] Z. Ding, X. Jiao, B. Yan, Y. Jia, and S. Guo, "Fall detection based on MIMO millimeter-wave radar," in *Proc. CIE Int. Conf. Radar (Radar)*, Haikou, China, Dec. 2021, pp. 3059–3063.

[22] F. Khan, J. W. Choi, and S. H. Cho, "Design issues in vital sign monitoring through IR UWB radar," in *Proc. 18th IEEE Int. Symp. Consum. Electron. (ISCE)*, Jun. 2014, pp. 1–2.

[23] Q. Wu, Z. Mei, Z. Lai, D. Li, and D. Zhao, "A non-contact vital signs detection in a multi-channel 77 GHz LFMCW radar system," *IEEE Access*, vol. 9, pp. 49614–49628, 2021.

[24] L. Sun, S. Huang, Y. Li, C. Gu, H. Pan, H. Hong, and X. Zhu, "Remote measurement of human vital signs based on joint-range adaptive EEMD," *IEEE Access*, vol. 8, pp. 68514–68524, 2020.

[25] H.-I. Choi, H. Song, and H.-C. Shin, "Target range selection of FMCW radar for accurate vital information extraction," *IEEE Access*, vol. 9, pp. 1261–1270, 2021.

[26] Q. Lv, L. Chen, K. An, J. Wang, H. Li, D. Ye, J. Huangfu, C. Li, and L. Ran, "Doppler vital signs detection in the presence of large-scale random body movements," *IEEE Trans. Microw. Theory Techn.*, vol. 66, no. 9, pp. 4261–4270, Sep. 2018.

[27] J.-M. Muñoz-Ferreras, Z. Peng, R. Gómez-García, and C. Li, "Random body movement mitigation for FMCW-radar-based vital-sign monitoring," in *Proc. IEEE Topical Conf. Biomed. Wireless Technol., Netw., Sens. Syst. (BioWireleSS)*, Jan. 2016, pp. 22–24.

[28] F. Wang, X. Zeng, C. Wu, B. Wang, and K. J. R. Liu, "Driver vital signs monitoring using millimeter wave radio," *IEEE Internet Things J.*, vol. 9, no. 13, pp. 11283–11298, Jul. 2022.

[29] F. Wang, F. Zhang, C. Wu, B. Wang, and K. J. R. Liu, "ViMo: Multiperson vital sign monitoring using commodity millimeter-wave radio," *IEEE Internet Things J.*, vol. 8, no. 3, pp. 1294–1307, Feb. 2021.

[30] A. Ray, A. Khasnobish, S. Rani, A. Chowdhury, and T. Chakravarty, "Exploration of mode decomposition for concurrent cardiopulmonary monitoring using dual radar," in *Proc. 28th Eur. Signal Process. Conf. (EUSIPCO)*, Amsterdam, Netherlands, Jan. 2021, pp. 1140–1144.

[31] A. Helzer, M. Barzohar, and D. Malah, "Stable fitting of 2D curves and 3D surfaces by implicit polynomials," *IEEE Trans. Pattern Anal. Mach. Intell.*, vol. 26, no. 10, pp. 1283–1294, Oct. 2004.

[32] M. E. Torres, M. A. Colominas, G. Schlotthauer, and P. Flandrin, "A complete ensemble empirical mode decomposition with adaptive noise," in *Proc. IEEE Int. Conf. Acoust., Speech Signal Process. (ICASSP)*, May 2011, pp. 4144–4147.

[33] K. Wang, Y. Zhao, and J. Fang, "Separation and denoising of respiratory heartbeat signals based on millimeter-wave radar," in *Proc. IEEE 4th Int. Conf. Power, Intell. Comput. Syst. (ICPICS)*, Shenyang, China, Jul. 2022, pp. 950–954.

[34] R. Ho and K. Hung, "A comparative investigation of mode mixing in EEG decomposition using EMD, EEMD and M-EMD," in *Proc. IEEE 10th Symp. Comput. Appl. Ind. Electron. (ISCAIE)*, Malaysia, Apr. 2020, pp. 203–210.

[35] C. Ding, J. Yan, L. Zhang, H. Zhao, H. Hong, and X. Zhu, "Noncontact multiple targets vital sign detection based on VMD algorithm," in *Proc. IEEE Radar Conf. (RadarConf)*, Seattle, WA, USA, May 2017, pp. 727–730.

[36] W. Yin, X. Yang, L. Li, L. Zhang, N. Kitsuwan, and E. Oki, "HEAR: Approach for heartbeat monitoring with body movement compensation by IR-UWB radar," *Sensors*, vol. 18, no. 9, p. 3077, Sep. 2018.

[37] M. Xiang, W. Ren, W. Li, and Z. Xue, "High-precision vital signs detection method based on spectrum refinement and extended DCMA," *J. Beijing Inst. Technol.*, vol. 31, pp. 101–111, Feb. 2022.

[38] P. Zheng, C. Zheng, X. Li, H. Chen, A. Wang, and Y. Luo, "Second harmonic weighted reconstruction for non-contact monitoring heart rate," *IEEE Sensors J.*, vol. 22, no. 6, pp. 5815–5823, Mar. 2022.

[39] Y. Wang, X. Wang, X. Lan, and Z. Han, "Vital signs monitoring using FMCW millimeter-wave sensor via simulated annealing MUSIC algorithm," in *Proc. 5th Int. Conf. Inf. Commun. Signal Process. (ICICSP)*, Nov. 2022, pp. 429–434.

[40] Z. Chen, Y. Liu, and Z. Cai, "Noncontact heart rate detection method based on Kalman filter," in *Proc. Global Rel. Prognostics Health Manage. (PHM-Yantai)*, Oct. 2022, pp. 1–5.

[41] M. Alizadeh, G. Shaker, J. C. M. D. Almeida, P. P. Morita, and S. Safavi-Naeini, "Remote monitoring of human vital signs using mm-wave FMCW radar," *IEEE Access*, vol. 7, pp. 54958–54968, 2019.

[42] H. Shen, C. Xu, Y. Yang, L. Sun, Z. Cai, L. Bai, E. Clancy, and X. Huang, "Respiration and heartbeat rates measurement based on autocorrelation using IR-UWB radar," *IEEE Trans. Circuits Syst. II, Exp. Briefs*, vol. 65, no. 10, pp. 1470–1474, Oct. 2018.

[43] M. Le and B. Van Nguyen, "Multivariate correlation of higher harmonics for heart rate remote measurement using UWB impulse radar," *IEEE Sensors J.*, vol. 20, no. 4, pp. 1859–1866, Feb. 2020.

[44] T. K. V. Dai, Y. Yu, P. Theilmann, A. E. Fathy, and O. Kilic, "Remote vital sign monitoring with reduced random body swaying motion using heartbeat template and wavelet transform based on constellation diagrams," *IEEE J. Electromagn., RF Microw. Med. Biol.*, vol. 6, no. 3, pp. 429–436, Sep. 2022.

[45] J. Wang, X. Wang, Z. Zhu, J. Huangfu, C. Li, and L. Ran, "1-D microwave imaging of human cardiac motion: An *ab − initio* investigation," *IEEE Trans. Microw. Theory Techn.*, vol. 61, no. 5, pp. 2101–2107, May 2013.

[46] M. Mercuri, Y.-H. Liu, I. Lorato, T. Torfs, F. Wieringa, A. Bourdoux, and C. Van Hoof, "A direct phase-tracking Doppler radar using wavelet independent component analysis for non-contact respiratory and heart rate monitoring," *IEEE Trans. Biomed. Circuits Syst.*, vol. 12, no. 3, pp. 632–643, Jun. 2018.

[47] C. Will, K. Shi, R. Weigel, and A. Koelpin, "Advanced template matching algorithm for instantaneous heartbeat detection using continuous wave radar systems," in *IEEE MTT-S Int. Microw. Symp. Dig.*, May 2017, pp. 1–4.
[48] M. Shahbakhti, M. Beiramvand, M. Nazari, A. Broniec-Wójcik, P. Augustyniak, A. S. Rodrigues, M. Wierzchon, and V. Marozas, "VME-DWT: An efficient algorithm for detection and elimination of eye blink from short segments of single EEG channel," *IEEE Trans. Neural Syst. Rehabil. Eng.*, vol. 29, pp. 408–417, 2021.
[49] N. U. Rehman and H. Aftab, "Multivariate variational mode decomposition," *IEEE Trans. Signal Process.*, vol. 67, no. 23, pp. 6039–6052, Dec. 2019.
[50] M. Nazari and S. M. Sakhaei, "Variational mode extraction: A new efficient method to derive respiratory signals from ECG," in *IEEE J. Biomed. Health Informat.*, vol. 22, no. 4, pp. 1059–1067, Jul. 2018.
[51] P. Bharti and Roshan, "High PSNR based image watermarking by DWT-CZT-SVD algorithm," in *Proc. 8th Int. Conf. Comput. Intell. Commun. Netw. (CICN)*, Tehri, India, Dec. 2016, pp. 404–407.
[52] M. Xiang, W. Ren, W. Li, Z. Xue, and X. Jiang, "High-precision vital signs monitoring method using a FMCW millimeter-wave sensor," *Sensors*, vol. 22, no. 19, p. 7543, 2022.
[53] P. Liu, S. Zhang, and J. Yao, "High precision ranging algorithm of FMCW radar based on FFT+FT," *Foreign Electron. Meas. Technol.*, vol. 38, no. 10, pp. 65–69, 2019.
[54] T. Li and Y. Tang, "Frequency estimation based on modulation FFT and MUSIC algorithm," in *Proc. 1st Int. Conf. Pervasive Comput., Signal Process. Appl.*, Harbin, China, Sep. 2010, pp. 525–528.
[55] K. Yamamoto, K. Toyoda, and T. Ohtsuki, "Non-contact heartbeat detection by MUSIC with discrete cosine transform-based parameter adjustment," in *Proc. IEEE Global Commun. Conf. (GLOBECOM)*, Abu Dhabi, United Arab Emirates, Dec. 2018, pp. 1–6.
[56] P. Stoica and A. Nehorai, "MUSIC, maximum likelihood and Cramer–Rao bound: Further results and comparisons," in *Proc. Int. Conf. Acoust., Speech, Signal Process.*, Glasgow, 1989, pp. 2605–2608.
[57] Y. Zhao, Y. Liu, and Z. Cai, "A novel scheme for vital sign detection with FMCW radar," in *Proc. Global Rel. Prognostics Health Manage. (PHM-Yantai)*, Yantai, China, Oct. 2022, pp. 1–6.
[58] Z. Zhang, Z. Pi, and B. Liu, "TROIKA: A general framework for heart rate monitoring using wrist-type photoplethysmographic signals during intensive physical exercise," *IEEE Trans. Biomed. Eng.*, vol. 62, no. 2, pp. 522–531, Feb. 2015.
[59] K. Liu, C. Ding, and Y. Zhang, "A coarse-to-fine robust estimation of FMCW radar signal for vital sign detection," in *Proc. IEEE Radar Conf. (RadarConf)*, Florence, Italy, Sep. 2020, pp. 1–6.
[60] X. Huang, Z. Ju, and R. Zhang, "Real-time heart rate detection method based on 77 GHz FMCW radar," *Micromachines*, vol. 13, no. 11, p. 1960, 2022.
[61] S. Iyer, L. Zhao, M. P. Mohan, J. Jimeno, M. Y. Siyal, A. Alphones, and M. F. Karim, "mm-Wave radar-based vital signs monitoring and arrhythmia detection using machine learning," *Sensors*, vol. 22, no. 9, p. 3106 2022.
[62] G. Beltrão, W. A. Martins, B. Shankar M. R., M. Alaee-Kerahroodi, U. Schroeder, and D. Tatarinov, "Adaptive nonlinear least squares framework for contactless vital sign monitoring," *IEEE Trans. Microw. Theory Techn.*, vol. 71, no. 4, pp. 1696–1710, Apr. 2023.

MIN ZHOU received the B.S. degree from Yantai University, Yantai, China, in 2021, where she is currently pursuing the master's degree with the School of Physics and Electronic Information. Her research interests include radar signal processing and vital sign detection.

YUNXUE LIU received the Ph.D. degree from Shandong University, Jinan, China, in 2009. He is currently a Full Professor with the School of Physics and Electronic Information, Yantai University, China. His research interests include millimeter wave radar signal processing, high-speed signal real-time processing, electronic countermeasures, and cognitive radio.

SHIE WU received the B.S. degree in electronic and information engineering from Yantai University, Yantai, China, in 2010, and the M.S. degree in electronic and communication engineering and the Ph.D. degree in information and communication engineering from the Beijing University of Posts and Telecommunication (BUPT), China, in 2013 and 2017, respectively. She is currently an Associate Professor with the School of Physics and Electronic Information, Yantai University, China. Her current research interests include radio resource management and computation offloading in mobile edge computing systems.

CHENGYOU WANG (Member, IEEE) received the B.E. degree in electronic information science and technology from Yantai University, China, in 2004, and the M.E. and Ph.D. degrees in signal and information processing from Tianjin University, China, in 2007 and 2010, respectively. He is currently an associate professor and a supervisor of master's students with Shandong University, Weihai, China. His current research interests include digital image/video processing and analysis, computer vision, artificial intelligence, and wireless communication technology.

ZEKUN CHEN (Member, IEEE) received the B.S. degree from Yantai University, Yantai, China, in 2020, where he is currently pursuing the master's degree with the School of Physics and Electronic Information. His research interests include radar signal processing and vital sign detection.

HONGFEI LI received the B.S. degree from Yantai University, Yantai, China, in 2021, where he is currently pursuing the master's degree with the School of Physics and Electronic Information. His research interests include machine learning, natural language processing, and vital signs algorithm.